Validation for CFD Prediction of Mass Transport in an Aircraft Passenger Cabin

A. J. Baker
S. C. Ericson
J.A. Orzechowski
K.L. Wong
University of Tennessee
Knoxville, TN 37996

R. P. Garner
Civil Aerospace Medical Institute
Federal Aviation Administration
Oklahoma City, OK 73125

November 2006

Final Report

NOTICE

This document is disseminated under the sponsorship
of the U.S. Department of Transportation in the interest
of information exchange. The United States Government
assumes no liability for the contents thereof.
_____

This publication and all Office of Aerospace Medicine technical reports are
available in full-text from the Civil Aerospace Medical Institute's publications
Web site:
www.faa.gov/library/reports/medical/oamtechreports/index.cfm

Technical Report Documentation Page

1. Report No. DOT/FAA/AM-06/27	2. Government Accession No.	3. Recipient's Catalog No.
4. Title and Subtitle Validation for CFD Prediction of Mass Transport in an Aircraft Passenger Cabin		5. Report Date November 2006
		6. Performing Organization Code
7. Author(s) Baker AJ,[a] Ericson SC,[b] Orzechowski JA,[b] Wong KL,[c] Garner RP [d]		8. Performing Organization Report No.
9. Performing Organization Name and Address [a] U. Tennessee, Engineering Science Graduate program [b] U. Tennessee, Computational Fluid Dynamics Laboratory [c] U. Tennessee, Joint Institute for Computational Science [d] Federal Aviation Administration, Civil Aerospace Medical Institute (former employee)		10. Work Unit No. (TRAIS)
		11. Contract or Grant No.
12. Sponsoring Agency name and Address Office of Aerospace Medicine Federal Aviation Administration 800 Independence Ave., S.W. Washington, DC 20591		13. Type of Report and Period Covered
		14. Sponsoring Agency Code

15. Supplemental Notes

Work was accomplished under approved cooperative research and development task.

16. Abstract

A joint project was established to validate computational fluid dynamics (CFD) as a quantitative methodology for prediction of the distribution of pathogens released into the environmental control system (ECS)-generated ventilation flowfield of an aircraft passenger cabin. Acquisition of the requisite experimental databases for three-dimensional velocity and contaminant distributions was accomplished in the FAA Civil Aerospace Medical Institute's (CAMI's) Aircraft Environmental Research Facility (AERF). The associated CFD simulations were conducted by the University of Tennessee CFD Laboratory staff, on the resident Beowulf PC cluster and/or the University of Tennessee Innovative Computing Laboratory SiNRG cluster, using both commercial and proprietary CFD computer codes. The results of this CFD validation project are reported herein.

17. Key Words Aircraft Airflow, CFD Analysis, Environmental Control System, Aircraft Cabin Airflow, Aircraft Ventilation Flowfield, Aircraft Contaminant Distribution	18. Distribution Statement Document is available to the public through the Defense Technical Information Center, Ft. Belvior, VA 22060; and the National Technical Information Service, Springfield, VA 22161		
19. Security Classif. (of this report) Unclassified	20. Security Classif. (of this page) Unclassified	21. No. of Pages 55	22. Price

Form DOT F 1700.7 (8-72) Reproduction of completed page authorized

EXECUTIVE SUMMARY

A joint project is established to validate computational fluid dynamics (CFD) as a quantitative methodology for prediction of pathogen transport via the environmental control system (ECS)-generated ventilation flowfield of a commercial aircraft passenger cabin. Acquisition of the requisite experimental database for three-dimensional velocity and gaseous contaminant distributions is ongoing in the FAA Aircraft Environmental Research Facility (AERF) under the auspices of the Civil Aerospace Medical Institute (CAMI). The CFD simulations are executed on the University of Tennessee CFD Laboratory Beowulf PC cluster, and/or the University of Tennessee Innovative Computing Laboratory SiNRG cluster, using both commercial and proprietary CFD computer codes.

The results of this CFD validation project, spanning two contract periods, are reported herein. The selected sonic anemometer experimental data protocol has proven most appropriate for measurement of the characteristically unsteady ventilation velocity field in an aircraft passenger cabin. Consequently, a firm knowledge base is established for characterizing factors affecting time-accurate, 3-dimensional CFD prediction of unsteady ventilation flowfields in the AERF, hence validation of CFD as an incisive technology for meeting technical goals.

The CFD mass transport validation component proved more challenging to interpret, due principally to limitations inherent in the experimental protocol and measurement equipment. Notwithstanding, specifically designed and executed CFD computational experiments do provide clear insight into aircraft cabin ventilation design issues dominating time-dependent mass transport, hence CFD simulation fidelity.

The computer demand distinction between the commercial-steady RaNS CFD codes and time-accurate CFD algorithms/codes is clearly a dominating factor in application to contaminant transport simulation in aircraft cabins. Using the combination of these capabilities appears most important, with the principal value of the steady codes being initial-condition generation for the ensuing time-accurate simulations.

The AERF proved to be an exceptionally valuable facility supporting acquisition of advanced knowledge affecting the fate of contaminants introduced into an aircraft passenger cabin. However, only the CFD component of this project progressed to evaluation in fully configured cabins, including seat rows and gaspers. Notwithstanding, these results, in total, provide the FAA with a firm understanding of key factors affecting aircraft cabin ventilation association with transportation safety issues. This knowledge base can contribute guidance on potential damage mitigation strategy assessments, should an event be detected.

Contents

VALIDATION FOR CFD PREDICTION OF MASS TRANSPORT IN AN AIRCRAFT PASSENGER CABIN

INTRODUCTION

Noxious material may be intentionally or unintentionally released into an aircraft cabin during flight. Reaction management for this potential disaster must be based on predictive quantitative methodologies applied to potential scenarios adversely affecting cabin environmental quality. The direct option would employ in-flight testing, but this approach is prohibitively expensive, logistically awkward, and generates strictly airframe platform- dependent results.

The alternative is to employ computational fluid dynamics (CFD) to generate approximate solutions of the differential equation systems associated with the conservation principles. Closure models for turbulence are included that describe momentum and mass transport by and within velocity fields associated with aircraft ventilation. As with all engineering models, confidence in predictive capability rests completely on validation of the selected methodology. The CFD challenge, unique to aircraft cabin mass transport simulation, is the low speed, modestly turbulent unsteady character of the associated flowfields. Specifically, by design, aircraft environmental control system (ECS) operation at cruise generates barely perceptible velocity field variations associated with their low volumetric (air-changes per hour, ACH) operation. While CFD is a validated methodology for prediction of high-speed aerodynamic flowfields, the intricacies of its application to this very subtle-type flowfield is a current research, hence validation, topic.

Systems for ventilating inhabited spaces are designed to produce flowfields barely discernible by an immersed individual, in meeting the requirement for "comfort" (c.f, 1). Nielsen presented the first CFD ventilation velocity field prediction in a 2-dimensional enclosure in 1974 [2]. Following the European lead [3,4], the 1990s produced a significant interest in ventilation velocity field CFD prediction, with American Society for Heating, Refrigerating, and Air-Conditioning Engineers *Transactions* being a publication vehicle of choice [5–9]. The inaugural CFD prediction of the 3-dimensional ventilation flowfield in an aircraft passenger cabin was published by Baker et al. [10], closely followed by Jones et al. [11]. The first CFD velocity field validation exercise for an aircraft cabin was reported at the 2003 *Ventilation* Conference [12].

To date, the authors are not aware of the publication of a validation exercise for mass transport in an aircraft passenger cabin environment. CFD exercises pertinent to mass transport prediction in inhabited spaces were reported by Baker et al. [13] and Memarzadeh [14]. CFD algorithm issues pertinent to mass transport prediction accuracy are summarized in Baker et al. [15].

Applications of CFD methodology to inhabited space flowfield prediction have employed computer codes of numerous origin, including commercial, national, and local research versions. The fundamental mathematical theory underlying these various CFD codes for predicting essentially incompressible flowfields is uniformly based on an iterative "pressure projection" concept. "SIMPLE" is the legacy name associated with this theory, and individual developments employ many variations thereon that distinguish specific codes. Williams and Baker [16] provided the definitive theory, enabling discerning analysis of the range of implementation options, which center on "computational" versus "genuine" pressure fields, hence boundary conditions for the associated Poisson equations.

An additional distinguishing character of pressure projection theory codes is the numerical diffusion scheme required to stabilize iterative convergence difficulties induced by the convective non-linearity contained in the parent Navier-Stokes (NS) momentum conservation principle. Commercial codes generally contain first-, second-, and third-order numerical diffusion options, and the instructions suggest that this sequence be utilized in generating a given solution. The University of Tennessee CFD Lab research and prototype production codes contain a calculus-derived, tensor product numerical diffusion operator, which is third-order with an adjustable coefficient [17], or fourth-order with a theory-fixed coefficient [18].

No "physics" assumptions are required to perform a laminar flow simulation. Time-averaging the NS equations leads to the Reynolds-averaged (RaNS) system, which exposes a (Reynolds) stress tensor for characterization of turbulent flow processes. The most common closure for RaNS conservation law systems is one of several two-equation "TKE" models, e.g., k-epsilon, k-omega [19, 20]. This adds a pair of non-linear, elliptic partial-differential equations requiring boundary condition specifications, especially on solid surfaces. The usual implementation avoids resolution of near-wall state variable variations via use of the "log law" similarity correlation [19]. An alternative closure model avoiding this issue is the Spalart-

Allmaras single-equation eddy viscosity transport model [21]. Commercial codes also purport to have a large eddy simulation (LES) option [22] that involves a spatial NS averaging operation that produces four stress tensors characterizing turbulence phenomena. The commercial codes used in this project simplify the theory to a single (Reynolds) stress tensor for closure modeling. An LES formulation requires execution using a time-accurate CFD algorithm.

For this project, CFD simulations have been conducted using two firmly established commercial codes [23, 24], and the University of Tennessee CFD Lab research and prototype-production CFD codes [25, 26]. The University of Tennessee CFD Lab codes are specifically designed to readily adapt to improved numerics and/or closure models as developed. The former very efficiently generate steady solutions for the RaNS system using either the TKE or Spalart-Allmaras closure models. For mass transport, or unsteady flowfield prediction, these codes also contain a second-order accurate time integration option that is much slower to execute. This option is required as well when executing, using the cited LES formulation with its closure model. The University of Tennessee CFD Lab codes operate only in time-accurate mode, for laminar flow, and for turbulent flow using a TKE closure model. All codes can execute in parallel.

EXPERIMENTAL PROTOCOLS

Velocity vector field measurements

The key issue is experimental acquisition of high quality, 3-dimensional velocity vector data to support CFD validation. For this project, experimental velocity field data were collected at the CAMI AERF, Figure 1, a retired Boeing 747-100. A review of appropriate experimental methodologies confirmed that a sonic anemometer best met requirements for time-accurate, 3-dimensional data collection. Such a system was acquired and installed in an isolated portion of the tourist passenger cabin with seat rows removed, Figure 2a). Each anemometer [27] simultaneously recorded the three cartesian components of the AERF ECS-generated ventilation velocity vector at data rates from 3 to 60 hz, plus the local temperature. Figure 2b) illustrates the designed data acquisition matrix in the cabin transverse plane, which was interrogated at the nominal seat row pitch along the entire axial span of the isolated cabin segment.

The sonic anemometer is particularly appropriate to velocity vector field measurement of ventilation type. The selected anemometer is sensitive to a velocity component magnitude of order 0.03 m/s in a nominally spherical sample volume with diameter the order of one centimeter [27]. The simultaneously acquired 3-dimensional data contains the true velocity vector time-history at each sample station. These data can then be time-averaged for determination of the RaNS mean flow component, which may itself be time-dependent, and the rms fluctuation distributed about the identified mean. This data operation can thus provide firm quantification of the level of "turbulence" in the ECS-distributed velocity field.

The velocity field experiment acquisition protocol for the AERF was designed to minimize the effects of drift over the lengthy data collection period. Once the anemometers were in place, the AERF ventilation system was energized and allowed to come to equilibrium. When this was determined to have occurred (after about 20 min), the data stream from each anemometer was recorded for 5 min. The experiment tree was then moved to a new location in the test matrix, with stabilization followed by the 5-min data-recording period. This operation was

Figure 1. FAA Civil Aerospace Medical Institute Aircraft Environmental Research Facility, Mike Monroney Center, Oklahoma City, OK.
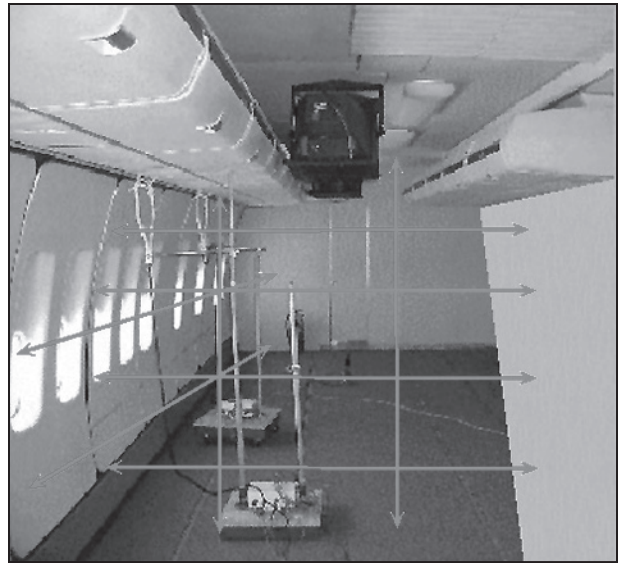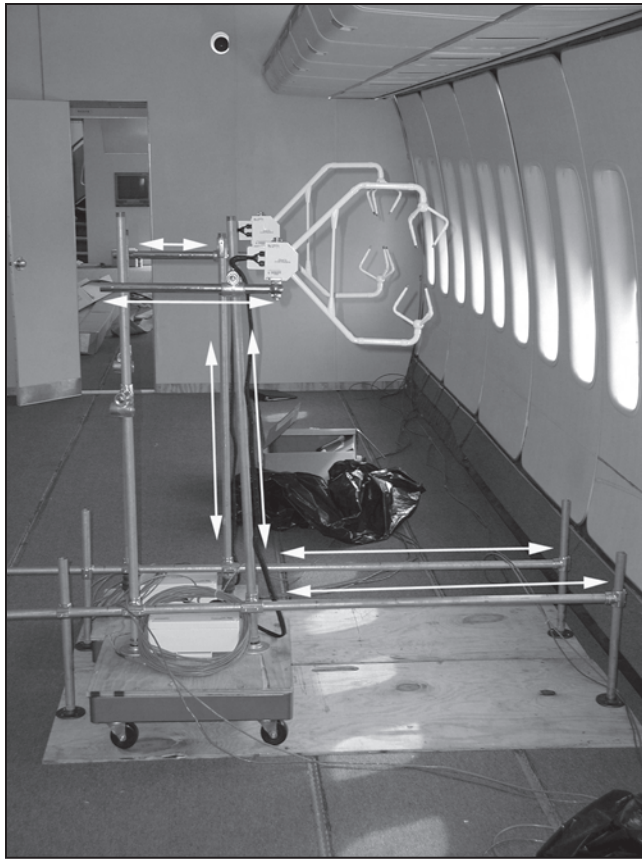
Figure 2. 3-D sonic anemometer installation in AERF. a) (left) velocity measurement sample volume with installation motion, b) velocity measurement grid map.

Figure 3. Graphic illustrating Boeing 747 ECS cabin ventilation supply plenum air introduction into passenger cabin. View facing cabin sidewall intersection with overhead luggage carrier.

Figure 4. Graphic illustrating introduction of VHP stream into AERF through nominal 4-in diameter duct. a) (above) global view facing cabin sidewall, b) (lower left) view upwards towards overhead luggage carrier, c) (lower right) view towards rear of cabin showing injection angle.
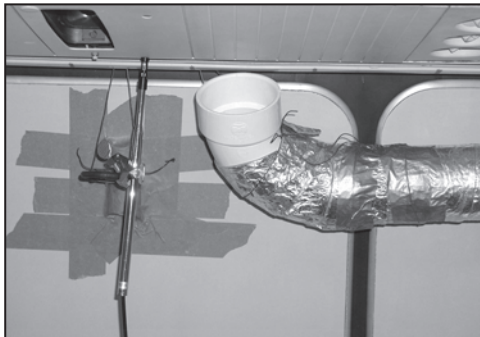
repeated at all locations on each cabin transverse half-plane over the length of the isolated cabin segment.

Figure 3 illustrates the wall jet character of the AERF ventilation supply flow. The physical size of the sonic anemometer head precludes velocity measurement in the wall jet region. Hence, flow speed in this region was recorded using a conventional hot wire from the supply plenum outflow face along and into the outer reach of the wall jet attached to the luggage carrier underside. Since flow in this region is unidirectional, conversion of speed to velocity vector is readily accomplished.

As the final component of aircraft cabin ventilation flow experimental measurements, the CAMI AERF sonic anemometer test apparatus was flown in a Boeing 747-400. The system measured the at-altitude cruise ECS-generated ventilation velocity vector field in locations above the elevation of the seat backs in the empty tourist section using the test protocol developed for the AERF. These data served as a validation base for the measurements obtained in the AERF using the identical experimental protocol.

Transported mass distribution measurements

The goal was to track a time-dependent mass species distribution within the AERF ventilation system flow field. This was accomplished by introducing vaporized hydrogen peroxide (VHP) into a cabin segment just aft of the aircraft entrance door in front of the wing. The cabin segment is 32 ft long and isolated by two bulkheads built specifically for the purpose. Tape and plastic sheeting were used throughout the cabin to minimize leakage during the tests, the details of which are summarized in [28].

VHP was introduced into the cabin at the terminus of the piping system shown in Figure 4a). The outlet from the generator passed into the cabin segment via a nominal 3-in diameter pipe penetrating the aft bulkhead. The pipe diameter was sized to ensure the VHP inflow velocity would exert minimum impact on the ECS-generated ventilation air introduction design. The aft bulkhead is the zero reference point of the z-axis of the Cartesian grid spanning the cabin segment. The VHP supply tube terminated in a 90-degree bend located $z = 108$ in from the aft bulkhead. The exit of the supply elbow, of nominal internal diameter 3.5 in, was centered 73 in above the floor (y direction), Figure 4b), with the normal coordinate of the exit face surface aligned at a nominal 45° angle with the horizontal, Figure 4c).

A single VHP generator was located outside the aft bulkhead, Figure 5a). The generator is a completely self-contained bio-decontamination system with the ability to dehumidify, generate vaporized hydrogen peroxide, and aerate sealed enclosures. The nominal generator operating condition was 35% solution of VHP in air at a rate of 12 g/min.

The time evolution of mass concentration level was acquired using a near-infrared spectrophotometer sensitive to both VHP and water vapor [29]. Figure 5b) presents a composite view of the experimental layout (Note: The fan was not in operation during these experiments). The sensors were attached to a vertical wire with x-z coordinates lying in the y-z plane of the center of the VHP supply elbow, (Figure 5c). Each measurement at each sensor coupon location involved a 10-min test period. The spectrophotometer data rate was 10 s, recorded via a serial RS-232 signal sent to a PC running LabVIEW data acquisition software [30]. Figure 5d) shows a pair of guided wave monitors with probe cells mounted.

COMPUTATIONAL PROTOCOLS

Geometry, mesh generation

The CFD simulation 3-dimensional solution domains are the product of the symmetric half-span of the AERF cabin segment with various cabin-axis spans selected such that boundary condition imposition did not interfere with simulation fidelity. The ventilation supply plenum runs the length of the fuselage, sandwiched between the sidewall and the sidewall-adjacent overhead luggage carrier. The cabin exhaust plenum also runs the length of the fuselage at floor level adjacent to the sidewall. Defining measurements were taken of all cabin interior features, the supply slot jet geometry, and the essential geometry of both the supply and exhaust plenums to the extent accessible.

The representative 3-D solution domain slice for CFD prediction of AERF velocity vector fields is graphed in perspective in Figure 6a). The supply plenum corresponds to the vertical appendage in the upper right side, while the exhaust plenum is the vertical appendage in the lower right corner. The rounded surface to the right is the fuselage sidewall, while the left vertical surface is the cabin symmetry plane. The contoured overhead luggage carriers appear as flow blockage insets in the solution domain. The external dimensions of the base CFD simulation domain block are approximately 100 in floor to ceiling, 120 in from sidewall to center plane, and 31 in axial span, the approximate seat row pitch. This domain block was then duplicated and appended as necessary to admit farfield boundary condition specifications pertinent to a specific test.

Extensive computational experience has solidly confirmed that the CFD solution domain must include portions of both supply and exhaust plenums to avoid boundary condition (BC) specifications in velocity
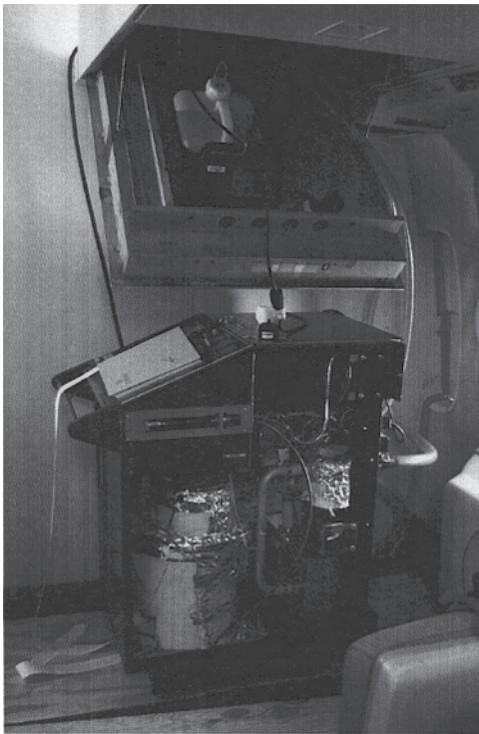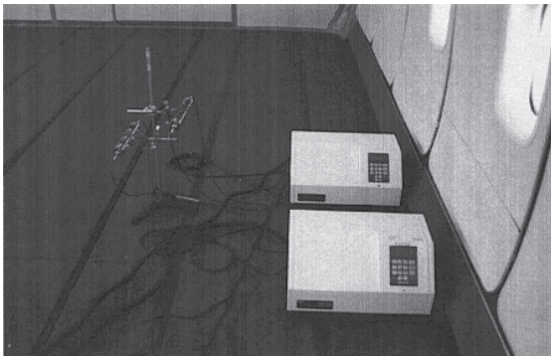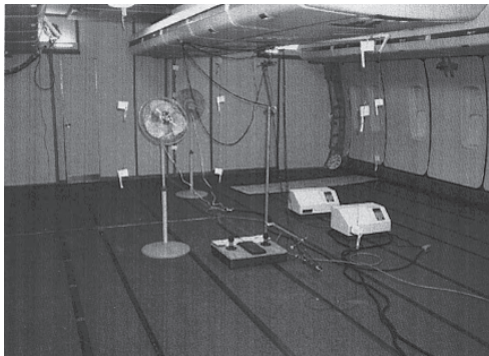
Figure 5. Steris VHP generation, distribution, and measurement system installation in AERF. a) (above left) VHP generator located exterior to cabin segment, b) (lower left) composite view of measurement system in cabin segment, c) (above right) hanger system for holding sample measurement coupons, d) (lower right) guided wave monitors with probe cells mounted.
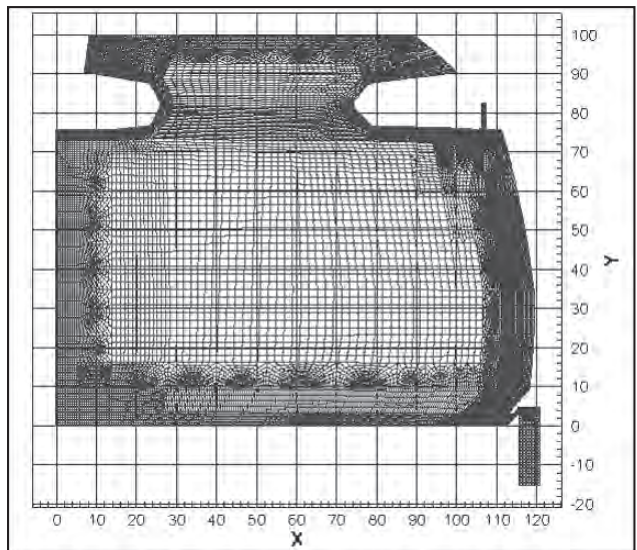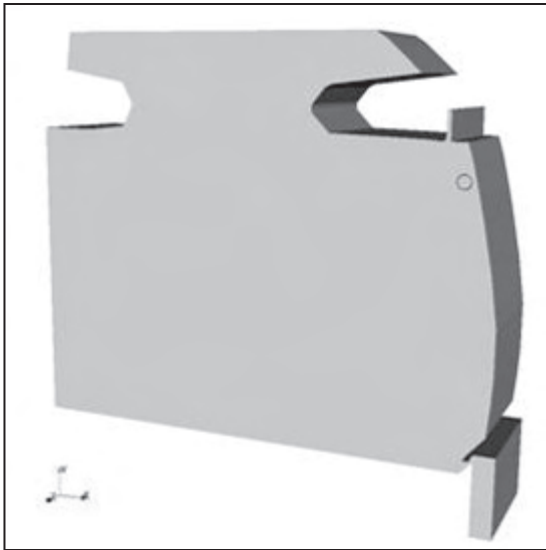
Figure 6. Generated computational mesh of hexahedron-shaped cells for a segment of the AERF cabin without seat rows. a) (left) perspective view illustrating geometric essence, b) planar cross-section showing solution-adapted, non-uniform meshing for local field resolution.
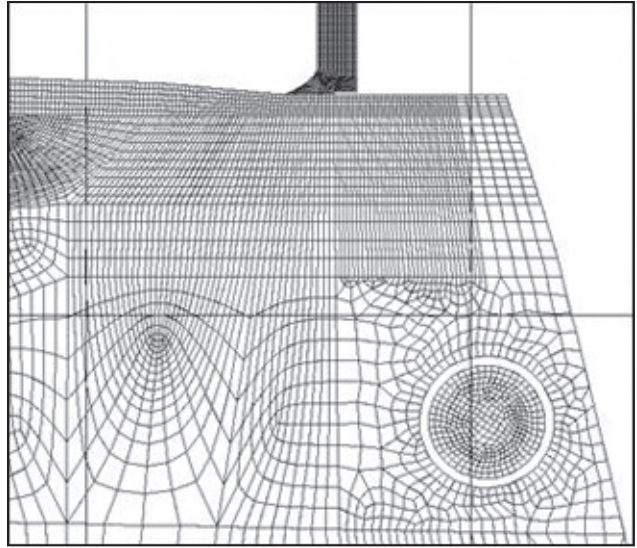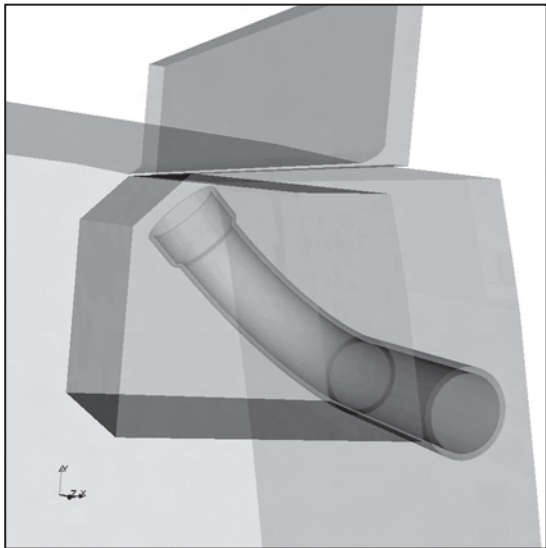

Figure 7. VHP terminus region mixed tetrahedron-hexahedron mesh. a) (left) perspective view illustrating geometric essence, b) planar cross-section showing solution-adapted non-uniform meshing for local field resolution.

7

merging-entrainment regions wherein the flow state is not *a priori* known. The inflow BC applied at the supply plenum entrance plane is a slug supply velocity and an assumed turbulence level. The passage length of the supply plenum is sufficient to convert this unimaginative BC into a solution to the RaNS equations prior to the flow becoming the supply slot jet. The BC specification appropriate at the exhaust plenum is uniform pressure and vanishing normal derivative for the velocity and turbulence closure variables across the outflow plane.

Following solution-adapted mesh alteration studies for wall jet and free jet resolution, the base hexahedral cell mesh discretization for the generic cabin slice containing both luggage carriers, rotated to a transverse plane view, is shown in Figure 6b). The resultant quite non-uniform mesh contained 14,300 nodes per mesh block plane. Baseline validation exercises employed one to nine co-joined blocks, uniformly spaced at 0.3 m intervals in the z-direction in the cabin region containing both luggage carriers. An 11-plane mesh was created to include the region where the central luggage carrier terminates. Therein, axial-direction non-uniform progression factors redefined z-plane spacing to provide axial mesh resolution in the central carrier terminus region, and domain meshing was added into the 3-D region that had been the interior of this luggage carrier.

The base cabin mesh block was then altered for inclusion of a mesh sub-block containing the VHP piping system and terminus, designed to induce minimal disturbance to the cabin ventilation supply slot jet flowfield (Figure 4). The injectant supply duct enters the CFD solution domain coincident with the small circle visible just below the supply plenum (Figure 6a). Figure 7a) presents a perspective view of the mesh block containing the injectant supply system terminus, which replaces the base mesh block. The flow in the 4-in diameter PVC pipe undergoes a terminal 90° turn, clearly visible therein, which introduces the injectant for entrainment into the wall-remote edge of the ventilation system wall jet attached to the overhead luggage carrier.

The VHP injection system terminus generates the need for a mixed mode discretization containing both hexahedron and tetrahedron-shaped computational cells. The tetrahedron "unstructured" meshing more readily enables the local refinements required for adequate resolution of flows about the quite non-regular geometry. Figure 7b) presents the generated mesh in a plane, rotated to planar view, just upstream of the 90° bend of the supply duct.

This piping-terminus system was designed to enable non-intrusive introduction of the VHP injectant. Data confirmed that the terminus face average velocity of the VHP was 0.7 m/s, which is quite modest compared to the supply slot jet average speed of 5 m/s. The injectant BCs were a slug velocity and assumed turbulence level at the entrance plane of the piping system, the circle in Figure 6a). The mass transport CFD simulation is required executed time accurate; therefore, the initial condition (IC) is mass fraction level at this plane and zero everywhere else.

CFD code selections

The CFD codes utilized in this study were two fully established commercial products [23, 24], the University of Tennessee CFD Lab academic research code [25] and the CFD Lab prototype production code jointly developed with JICS [26]. All codes are based theoretically on the pressure projection algorithm; the former two use a SIMPLE-variant finite volume discrete implementation, while the latter two employ the Williams finite element discrete implementation. The commercial and prototype production codes can handle both structured and unstructured meshes, constituted of unions of hexahedron and/or tetrahedron shaped cells. The academic research code is restricted to hexahedron meshes.

EXPERIMENTAL RESULTS

Velocity field measurements

The sonic anemometer protocol recorded the time history of ventilation velocity vector distributions in the AERF cabin segment. Design of the Boeing 747 ventilation system relies on the "Coanda effect" (one-sided entrainment) to maintain supply wall jet attachment to the underside of the overhead luggage carrier until reaching the carrier terminus upward turn (Figure 4a). Thereat, the wall jet separates, forming a large circulation region spanning the entire cabin half-space. In that portion of the cabin segment containing both sidewall and central luggage carriers, a second circulation region is created above the main circulation, which is confined to the region between the two luggage carriers. Via uniformity of the supply and exhaust plenums, the AERF ventilation supply system was designed to induce minimal axial flow along the cabin axis.

The orientation of the measurement planes with coordinate system is illustrated in Figure 2a). Three-dimensional velocity vector data were acquired on 10 planes transverse to the cabin axis spanned by the z-coordinate. At each transverse plane measurement location, the experimental recording rate was 3 samples/s over the 3-5 min recording window. The raw data were subsequently averaged over the four 30-s intervals, in the 3 – 5 min window, yielding totally time-independent cabin ventilation velocity vector field data sets.
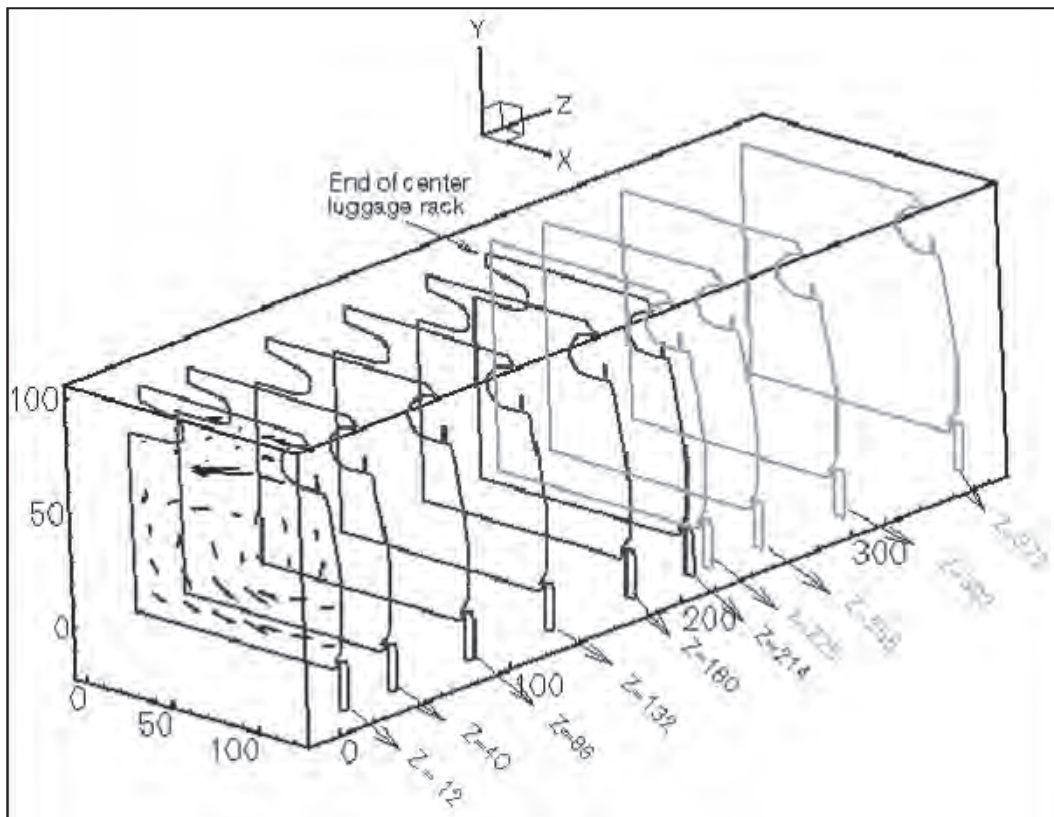
Figure 8. Perspective presentation of velocity vector experimental data planes in the AERF cabin segment devoid of seat rows.

The composite perspective view of the cabin segment velocity measurement planes is presented in Figure 8. Only one plane of data is visible in the still image, which is representative of all plane data clearly visible in the data set animation. Planar presentation of the totally time-averaged velocity data at z-stations in the middle of cabin segment containing two luggage carriers, and at 9-in after termination of the central luggage carrier, is given in Figure 9 a)-b). The length of each vector corresponds to its magnitude, and the 2 m/s reference scale vector is present in each graphic near the supply plenum profile.

Each z-station data set fully confirms the ventilation system design features. The separated wall jet clearly penetrates the cabin to the central luggage carrier, or cabin centerplane, creating a counter-clockwise circulation region filling the entire cabin half-span front to rear. A smaller, clockwise-rotating circulation region is generated in the cabin upper region bounded by the sidewall and central luggage carriers, where they both exist. The cabin circulation pattern does not exhibit significant z-dependence, as this measured component of the 3-D velocity vector was everywhere below instrument sensitivity, even in the near vicinity of the central luggage carrier terminus.

For experimental protocol validation, the complete AERF anemometer system was flown in a fully cabin-configured Boeing 747-400 to measure select ventilation velocity vectors at cruise and altitude. Figure 10 presents the data sample coordinates, all of which are above seated head height, referenced to a CFD mesh of the AERF. The data acquisition rate was 60 hertz over a span of 5 min. Figures 11a)– e) graph the time evolution of these data, resolved over 1-s intervals into the unsteady mean flow and the rms variation about the determined mean. Each graph has superimposed a fifth-degree, running-smoothing polynomial of the resolution. The mean flow in each instance is time-varying, with period of order min, while the rms fluctuations appear time-invariant and essentially isotropic and homogeneous.

The measured aircraft ECS-generated cabin ventilation velocity vector fields, in both the CAMI AERF and the Boeing 747-400 inflight test, led to a consensus summary containing the following observations:

The mean ventilation velocity vector field is time-varying with unsteadiness period on the order of a min.

Resolution of the 3-D 60 hertz velocity vector field measurements into time-unsteady mean and rms fluctuating components indicated the turbulence field is isotropic, homogeneous, and essentially time independent.
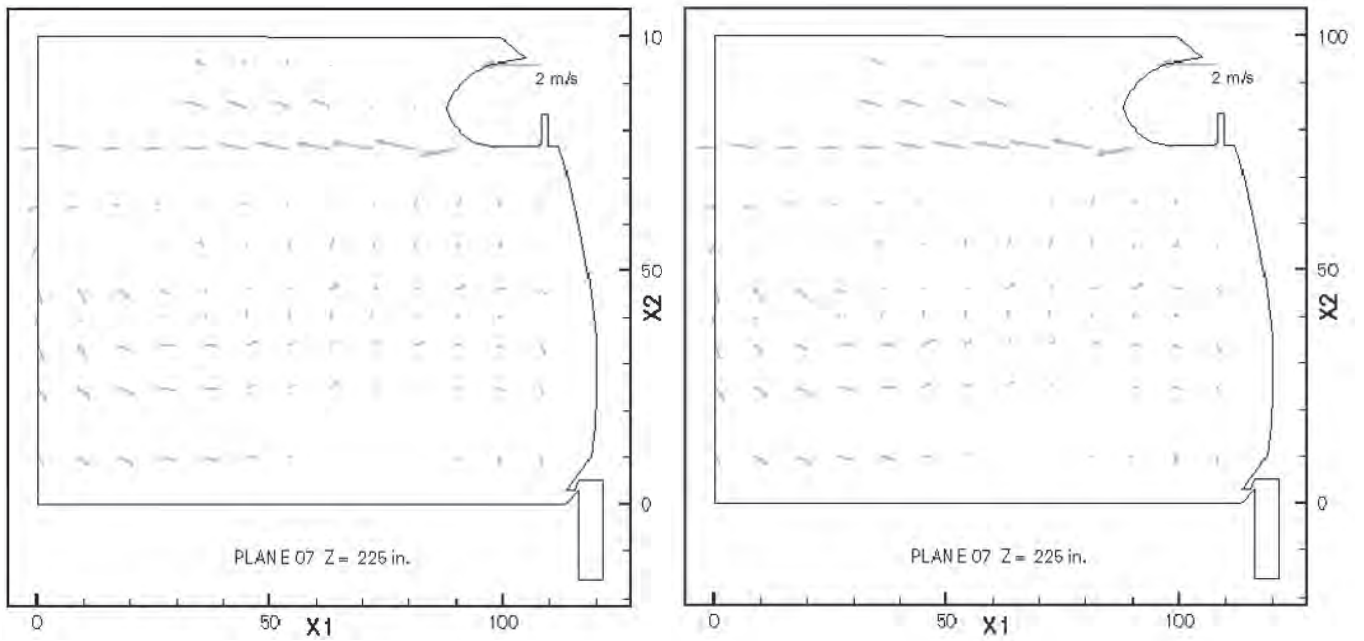
Figure 9. Experimentally measured totally time-averaged ventilation velocity vector distributions, AERF cabin segment transverse planes without sear rows. a) (left) plane Z=86 containing both overhead luggage carriers, b) plane Z=226 with only the sidewall overhead luggage carrier.
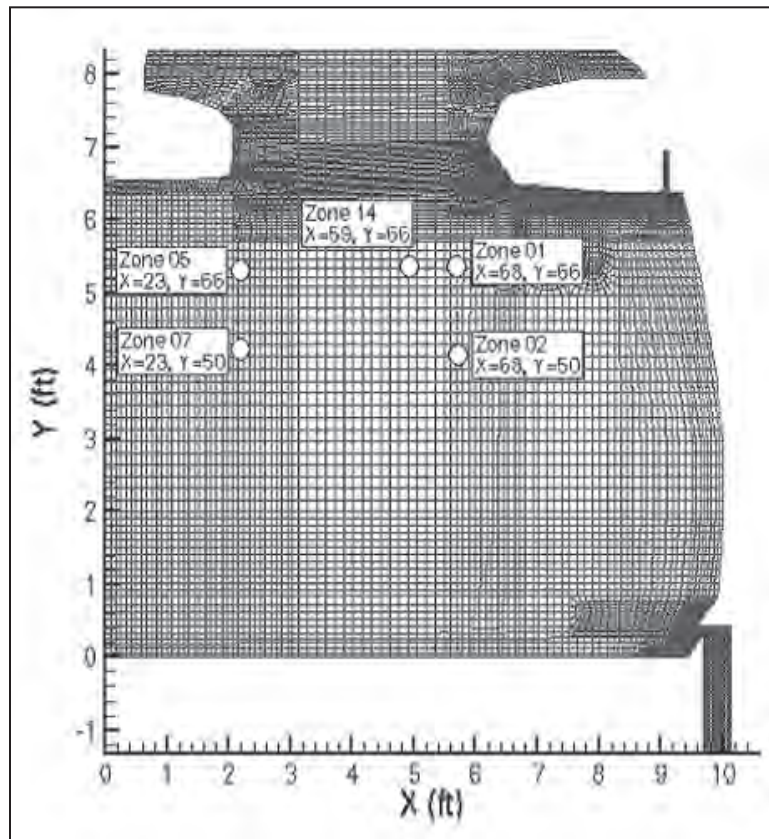

Figure 10. Location of ventilation velocity vector sample points during Boeing 747-400 inflight cruise at altitude test, projected onto a planform of the AERF.
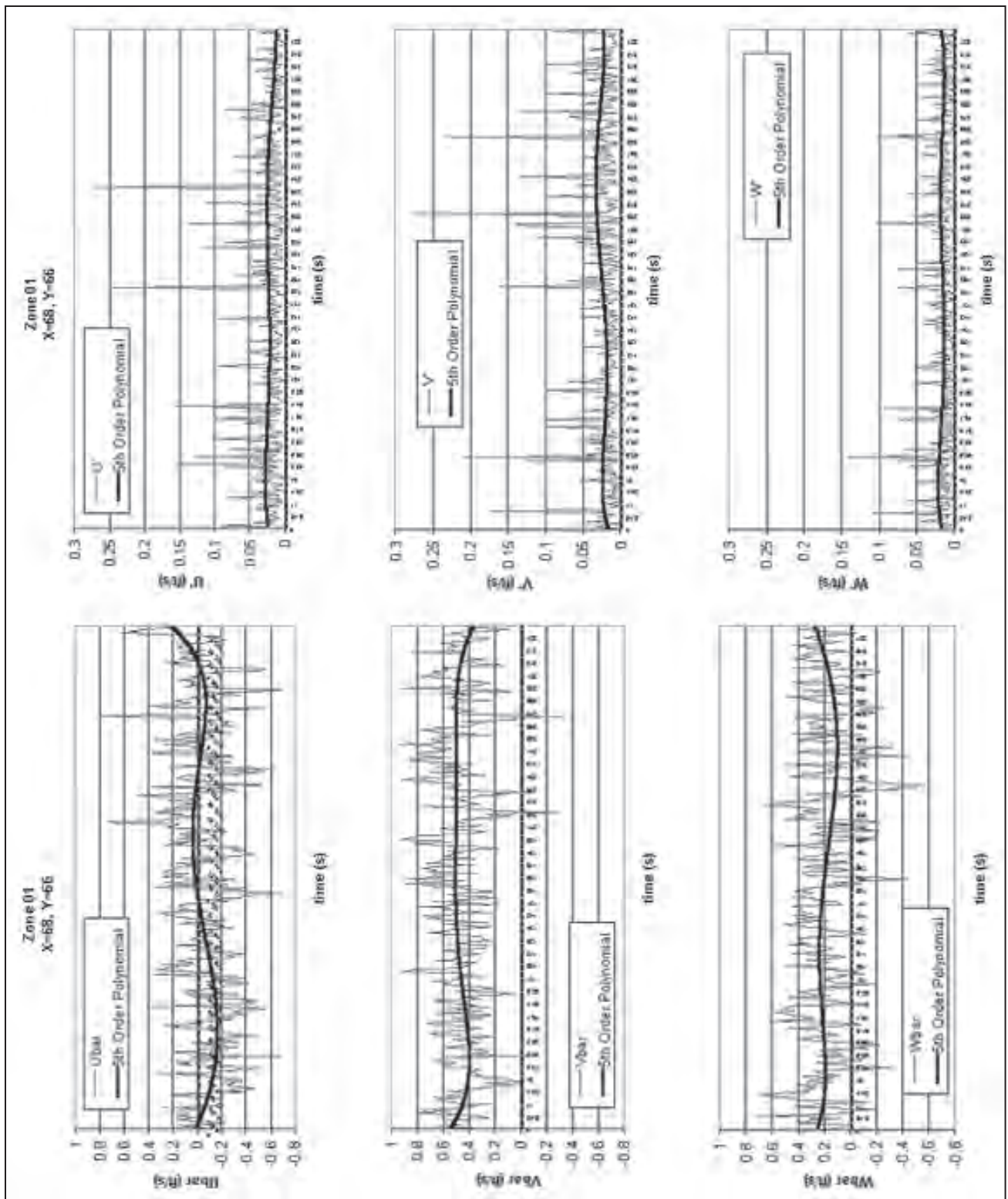
Figure 11a. Measured time-dependent ventilation velocity fields during inflight. Left column is time-dependent, mean velocity vector scalar resolution; right column is rms fluctuating velocity vector scalar resolution. a) zone 1, b) zone 2, c) zone 5, d) zone 7, e) zone 14.
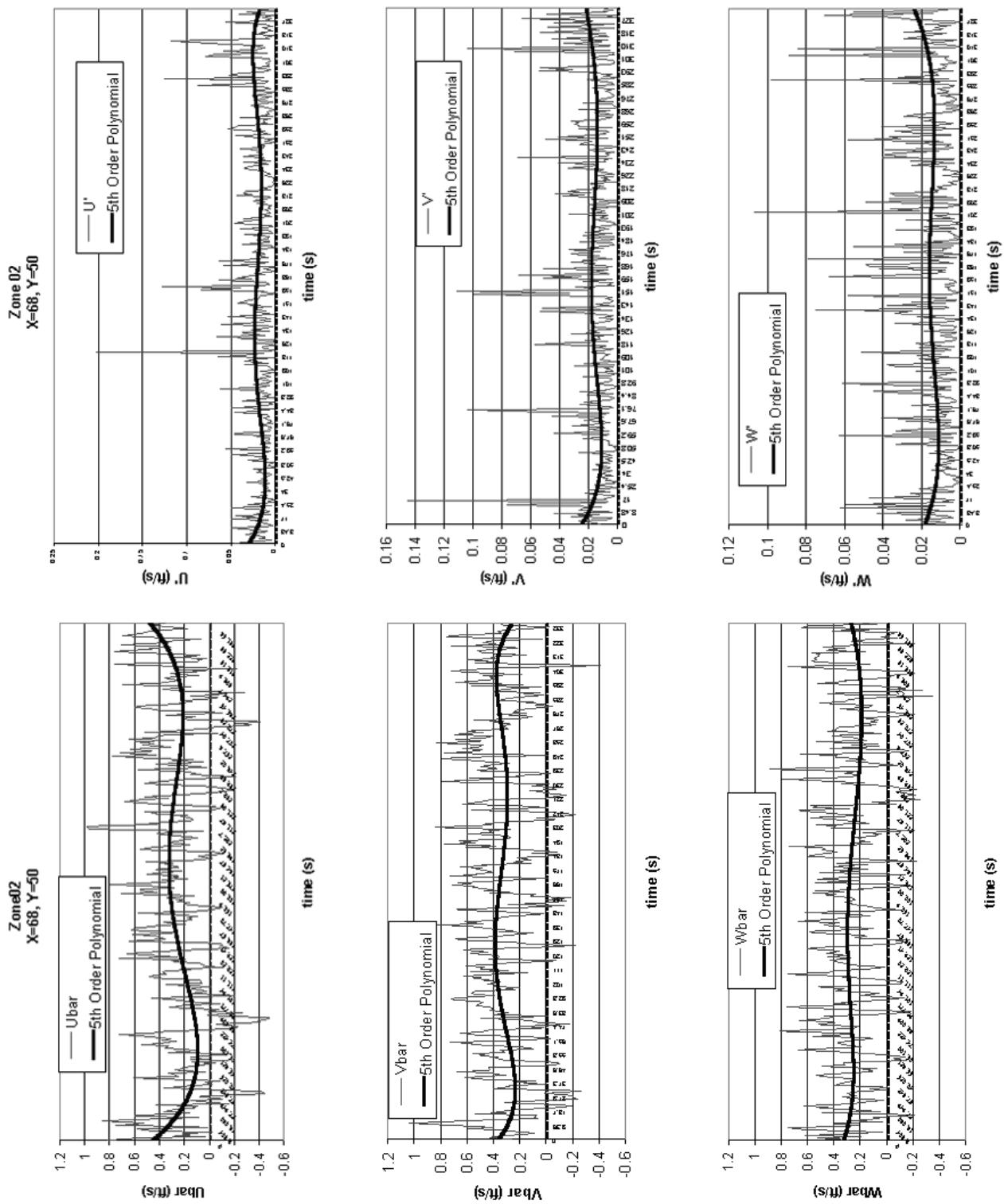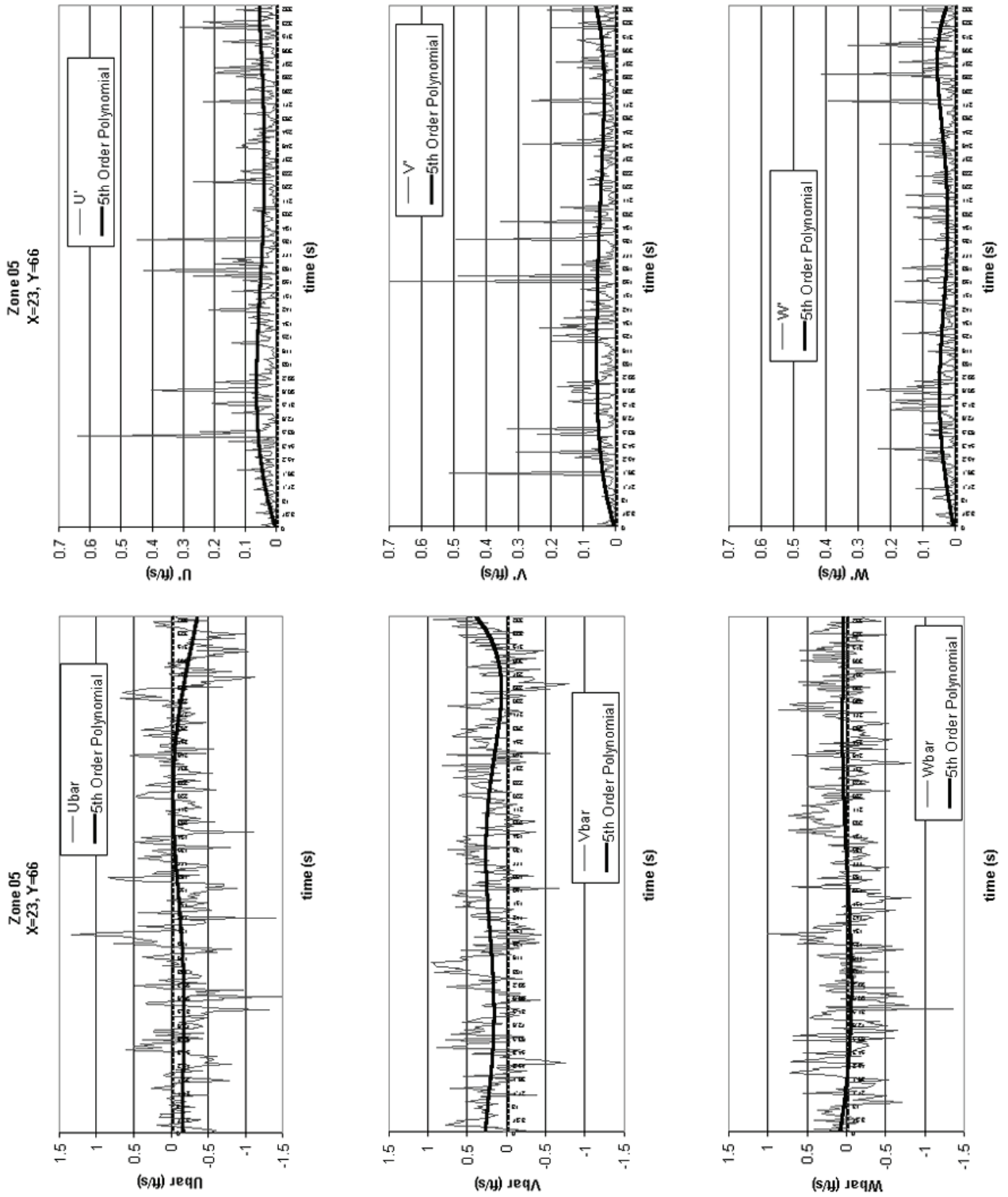
Figure 11b. Measured, time-dependent ventilation velocity fields during inflight experiment; left-column is mean velocity scalar resolution, right column is RMS fluctuating velocity scalar resolution.
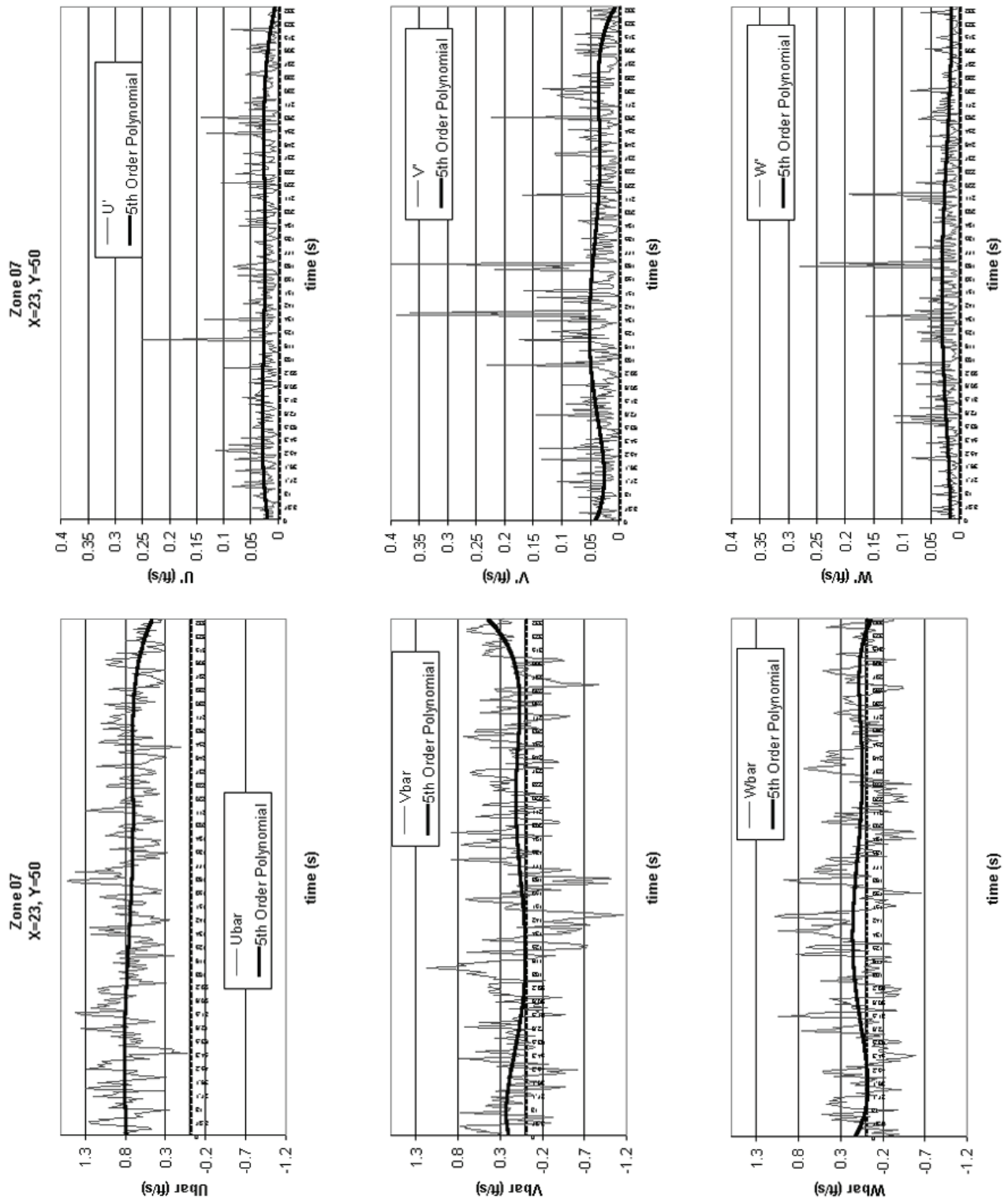
Figure 11c. Measured, time-dependent ventilation velocity fields during inflight experiment; left-column is mean velocity scalar resolution; right column is RMS fluctuating velocity scalar resolution.
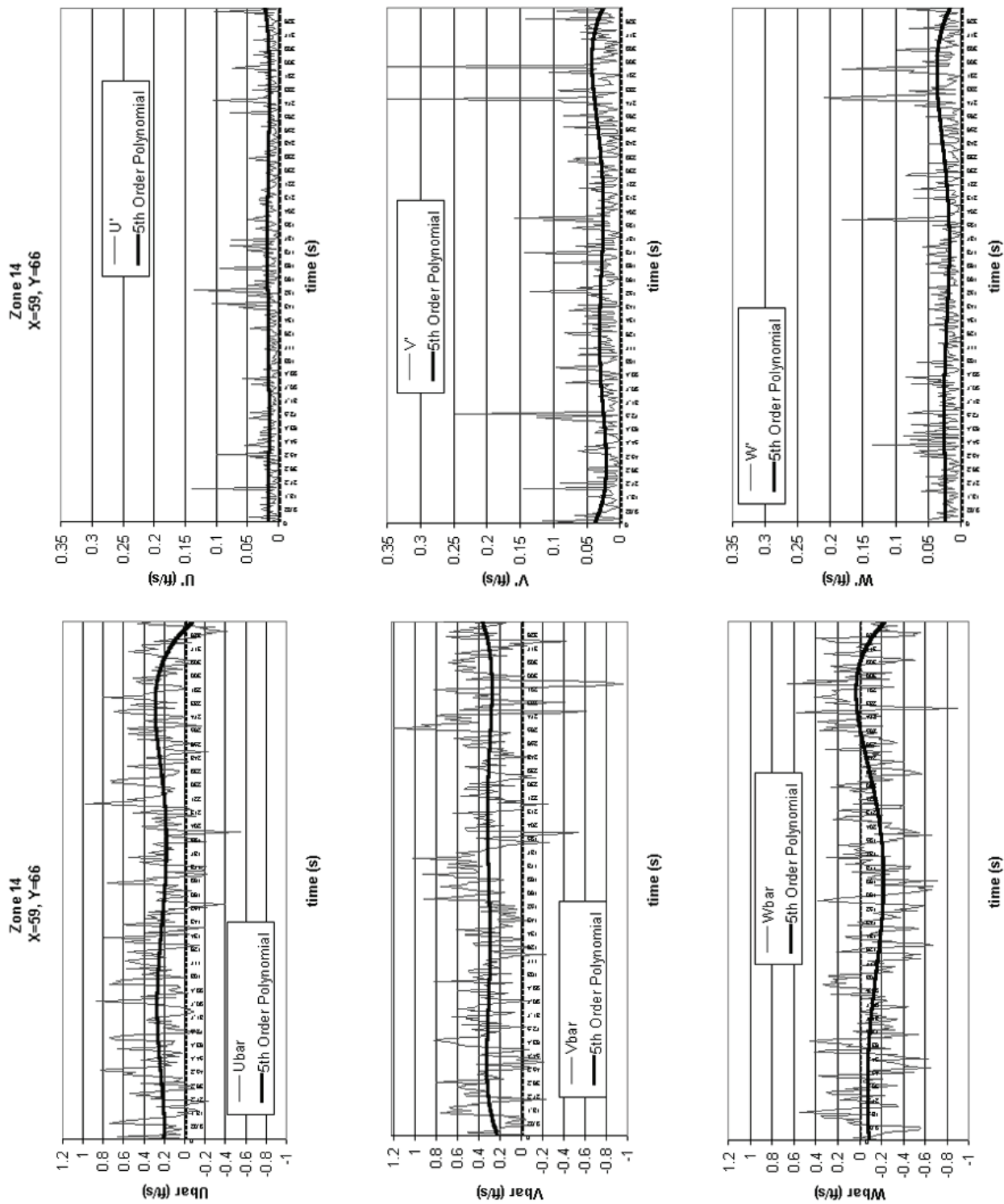
13

Figure 11d. Measured, time-dependent ventilation velocity fields during inflight experiment, left-column is mean velocity scalar resolution; right column is RMS fluctuating velocity scalar resolution.

14

Figure 11e. Measured, time-dependent ventilation velocity fields during inflight experiment; left-column is mean velocity scalar resolution; right column is RMS fluctuating velocity scalar resolution.

Conversely, the resolved time-varying mean velocity vector field is not isotropic or homogeneous and dependent on location within the cabin.

For the AERF ventilation rate of 40 ACH (air changes/hour), the mean velocity jet issuing from the supply plenum slot nozzle is order 5 m/s, which decays to order 1 m/s just downstream of wall jet separation from the luggage carrier underside.

After wall jet separation, the resultant free jet maintains coherence and momentum in traversing the cabin half-span distance, with the totally time-averaged mean velocity vector disposed to a slight upward arching.

The totally time-averaged mean flow speed within the cabin large circulation path decays from order 1 m/s to order 0.25 m/s.

The nominal speed associated with time-average rms fluctuation velocity is order 0.025 m/s; the corresponding turbulence kinetic energy level k is order 0.01 m^2/s^2.

For nominal circulation path mean speed ranging 1 - 0.25 m/s, the percentage of kinetic energy residing in the rms (turbulence) velocity field ranges 2 – 10 % .

Mass transport measurements

The design of the mass injection system was successful in not significantly altering the cabin ventilation velocity vector field (Figure 9). Therefore, data acquisition design called for measurement of VHP and/or water vapor concentrations along the nominal trajectory of the ventilation free jet traversing the upper cabin and continuing along the circulation path to the cabin floor. Figure 12 shows the VHP sample measurement locations on the platform of the cabin CFD solution domain.

Figure 13 presents the spectrophotometer-measured raw data for VHP concentration at the first four sample
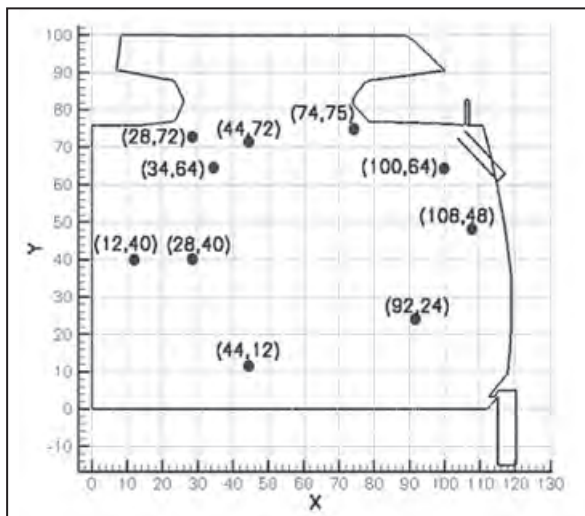

Figure 12. Transverse plane coordinates of sample locations for VHP measurements in the AERF.

locations along the free-jet trajectory as a function of time (min). On each graph, the dotted red line denotes the VHP generator being turned on and off. The diamond symbols correspond to each data point recorded at the system 10-s sampling interval. The solid blue line is a 30-s running-smoothing interpolation of the raw data.

Viewing these four data sets, the VHP concentration level decreases along the cabin circulation path as expected. A steep rise in VHP concentration is recorded at the sample point nearest to wall jet separation, Figure 13a), and a quite solid, steady-state level results with minimal data spread. In proceeding along the ventilation circulation path, the spread of the raw data about the running-smoothing mean monotonically increases as the onset rise progressively weakens. At the last two sample points nearest the central luggage carrier (Figure 12), the raw data fluctuation spread is on the order of the mean, which makes the mean a less representative data summary. This issue totally dominates the data further along the cabin circulation path, so these sample-point data were not further considered.

DISCUSSION AND RESULTS

CFD velocity field prediction specifications

AERF cabin flowfield simulations were principally conducted using one commercial code [23] and the cited research CFD codes [25, 26] for a range of turbulence closure models. Select simulations were executed using a second commercial code [24] for cases encountering anomalous solution behavior. All computations were 3-D on the described cabin symmetric half-geometry, as enabled by enforcing a symmetry boundary condition (BC) on the cabin mid-plane. The axial spans of the CFD solution domains ranged 0.3 - 5.0 m. All solution domain enclosing solid surfaces employed the no-slip BC for velocity. The AERF 40 ACH ventilation rate produces a nominal 5 m/s supply slot velocity magnitude; the corresponding Reynolds number per unit length is Re/L ≈ 1.5 E05/m, while Re ≈ 4 E03 is based on supply plenum data.

For CFD simulations using the two-equation TKE turbulence closure model, the law-of-the-wall BC was employed. This approximation [16] replaces wall layer mesh resolution requirement with a boundary layer-based estimation of k and ε within a restricted distance from a solid surface. When using the one-equation closure model, the BC is eddy viscosity vanishing on solid surfaces. No special treatment for solid surfaces was requested as input specification for the commercial code LES models. These codes employ the simplest (box filter) LES implementation, and coalesce the four theory-generated Reynolds stress tensors into a single (dissipative only) tensor closed
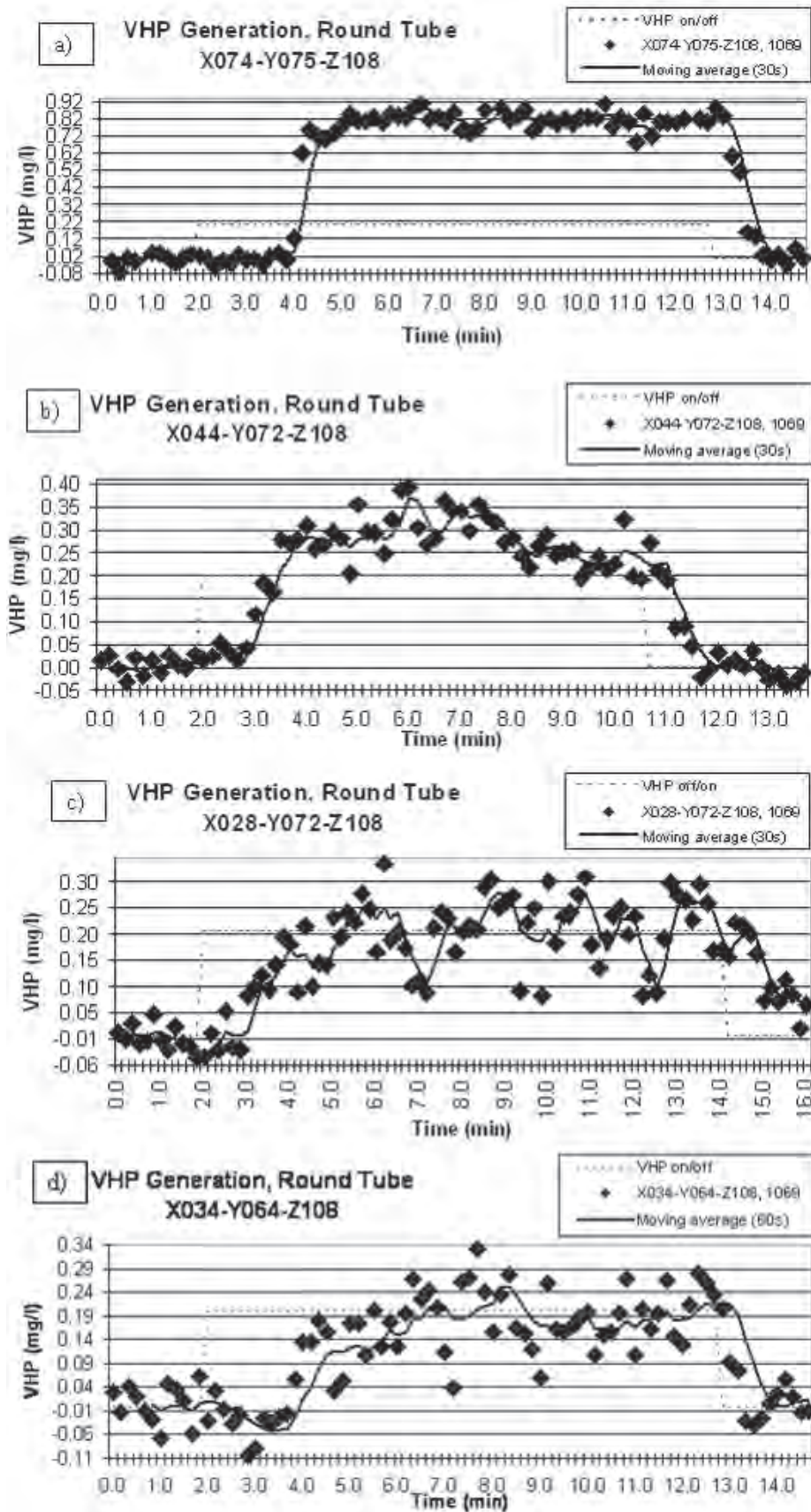
Figure 13. Time evolution of VHP concentrations measured at sample locations in the AERF. Plane Z=108, a) X=074, Y=075, b) X=044, Y=072, c) X=028, Y=072, d) X=034, Y=064.

with the Smagorinsky subgrid scale (SGS) mixing length theory (MLT) eddy viscosity model.

Simulations were also conducted using no turbulence model, i.e., laminar flow. Interestingly, the PDE form of laminar NS is identical to that produced by the LES box implementation, upon omitting the Smagorinsky closure model. All simulation CFD models, i.e., NS, RaNS, and LES, require stabilization generated by a numerical diffusion mechanism uniquely intrinsic to each code. Therefore, it is the interaction between numerical and physical model diffusion processes that ultimately leads to a solution.

Baseline cabin CFD velocity field validation

Baseline velocity field CFD simulations were conducted in the absence of the VHP injection system, on solution domains constituted of 1 to 9 axial mesh blocks. For vanishing derivative BCs specified on the associated domain axial end planes, all solutions generated flow fields that were numerically two-dimensional, as expected. Conversely, inclusion of the VHP injection system generates a local, modestly three-dimensional flowfield.

For the laminar flow assumption at Re=4 E03, the commercial code [23] produced a steady solution using the first-order numerical dissipation option with execution time a matter of hours. The second- and third-order dissipation option continuations did not yield algorithm convergence. This first order laminar flow solution velocity field is summarized in Figure 14 as a color contour flood of speed. It exhibits good agreement with all essential aspects of the fully time-averaged experimental data (Figure 9a) as the Coanda-effect wall jet separates from the luggage carrier terminus and proceeds as a free jet across the entire cabin half-span, including a slight upwards arching.

The production research code [26] unsteady time-accurate laminar flow simulation, at Re=E03 and stabilized via its second order numerical dissipation model, generated a time-accurate solution through ~20 s elapsed time, comparatively requiring several days of computer time. This solution never achieved a steady state, the result of the wall jet separation at the luggage carrier terminus being time varying. Thereby, the free jet trajectory oscillated about the mean velocity unit vector pattern (graphed in Figure 15a) as uniform length (unit) vectors colored by speed. This presentation format enables visualization of the main cabin circulation pattern, filling the half-space, and the smaller clockwise circulation pattern bounded laterally by the luggage carriers. (This is preferred to the conventional vector presentation where vector length denotes velocity magnitude, as the graphic is overwhelmed by the length of slot jet vectors.) A magnified view of the slot jet region velocity distribution (Figure 15b) clearly shows smooth flow turning and acceleration through the
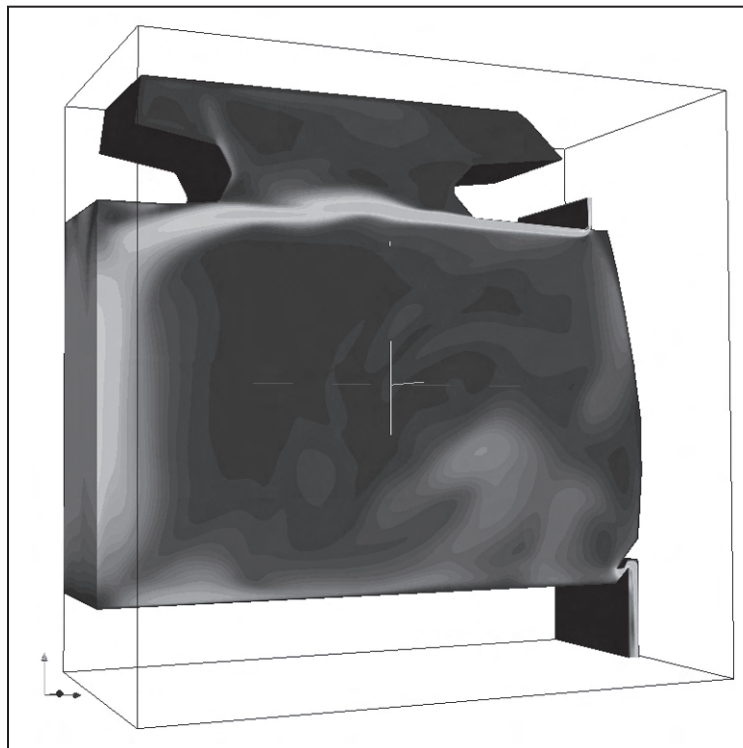

Figure 14. Fluent generated ventilation velocity field in AERF cabin section. Z=86 with both overhead luggage carriers, steady laminar flow simulation, Re = 4 E 03, 3-dimensional velocity vector magnitude colored by speed.
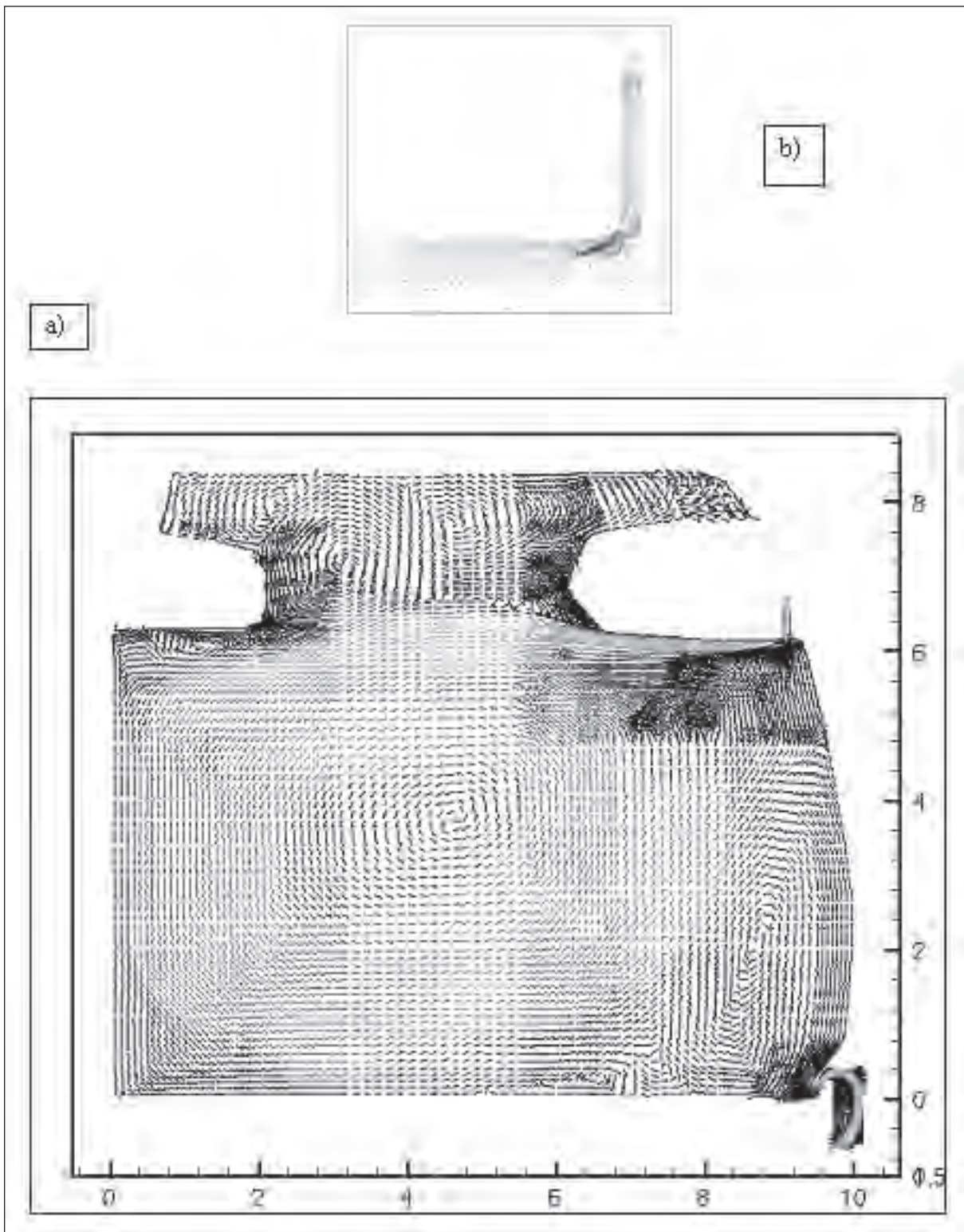
18

Figure 15. Transverse plane presentation of PICMSS generated ventilation velocity field in AERF cabin section, Z=86 with both overhead luggage carriers, unsteady laminar flow simulation, Re/L = E 03, a) velocity unit vectors colored by speed, b) magnification of velocity unit vectors in supply plenum-slot jet region.

slot, and this solution exhibits all essential aspects of the fully time-averaged experimental data (Figure 9a).

Using the TKE closure model and first-order numerical diffusion, the primary commercial code generated a steady velocity field distribution, again in a matter of hours. This TKE simulation did not predict wall jet separation at the luggage carrier terminus. Instead, the wall jet remained attached to the luggage carrier surface past the tangent break (recall Figure 2), hence it formed a single counter-clockwise circulation pattern reaching from cabin ceiling to floor.

The desired separation location was forced by moving an axial mesh node row to create a "trip strip" at the luggage carrier tangent break. The resulting TKE solution, sequencing through the first- and second-order numerical dissipation options, produced the steady velocity vector field, graphed as unit vectors colored by speed in Figure 16a). This solution also evidences essential agreement with the totally time-averaged data, including the slight upwards arching evident in the experimental free jet (Figure 9). Figure 16b) magnifies the slot jet region velocity distribution, while Figure 16c) is a highly magnified view of the mesh trip strip with local meshing density. The commercial code iterative process did not converge, for this TKE solution restarted using the third-order dissipation option.

Cabin mesh refinement CFD study

This result prompted a mesh refinement study focused on resolution of the luggage carrier terminus smoothly rounded profile, Figure 2. Figure 17a) graphs the mesh resolution improvement for the carrier curved terminus (red) and its sharp corner approximation (blue) resultant for mesh densification from 14,300 to 16,250 nodes per plane. Figure 17b) compares the sharp terminus (red) to a tangent approximation to the genuine curved surface (blue). The resultant commercial code second order dissipation option TKE solution transverse plane circulation patterns, colored by speed, are graphed in Figure 18. Both TKE solutions, for the genuine curvature and its tangent approximation, fail to predict flow separation at the luggage carrier terminus, leading to a single cabin circulation pattern. Conversely, the mesh with sharp corner approximation does lead to prediction of the correct separation phenomena, Figure 19, without the radical distortion originally used (Figure 16c).

This result is fundamentally disturbing, as one basically must know the correct solution to generate the accurate CFD approximation! To test whether this is solely the attribute of the base commercial code, the second commercial code [24] was executed using the identical sharp and curved terminus refined meshes. Turbulence closure remains the standard TKE model with wall function BCs. The solution process was cycled through the suggested sequence of numerical dissipation options (Prelax=0.1, 0.2, 0.3), for which the resultant velocity fields were visually indistinguishable. Figure 20 presents the luggage carrier rounded corner and sharp corner solutions, graphed in perspective as glyph velocity vector maps colored by speed, which fully confirms that the erroneous solution is not code-dependent.

The requirement that the luggage carrier terminus be geometrically sharp is due to perhaps three attributes of these commercial code simulations. Primary may be use of the log-law approximation for TKE model BCs on the carrier, intrinsic to which is the assumption of an attached boundary layer flow. The replacement of the log-law BCs with no-slip BCs would require extensive mesh refinement throughout the entire wall jet region to accurately implement a low turbulent Reynolds number TKE model. This, in turn, would substantially increase mesh nodalization, with an attendant increase in computer execution time. A second contributing factor may be excessive numerical diffusion, although the suggested dissipation model cycling did not impact the erroneous solution generation. Finally, both commercial codes employ an iteration procedure designed to generate a steady solution, hence the selected numerical linear algebra process may be the dominating factor.

To evaluate these hypotheses, the academic research code executed a time accurate, unsteady TKE simulation on the original, single-width base mesh block (14,300 nodes per plane). The mesh trip non-smooth node row (Figure 16c) was moved back to yield a sharp terminus, identical to that for which the commercial code simulation failed on this mesh. The TKE log-law BC definition was retained on the luggage carrier underside. The simulation initial condition (IC) was the commercial code steady TKE solution for the mesh with trip-strip (Figure 16a).

The velocity vector field immediately became time dependent, the result of wall jet separation unsteadiness from the luggage carrier terminus. Using the TKE log law BC, wall-jet separation remained located at the carrier terminus tangent break. Snapshots of the time evolution of transverse plane speed distribution over 40 s of simulation time are graphed in Figure 21. The color spectrum is distorted to enhance visualization of the wall jet transition to the free jet in the near field (wherein red to yellow now appear). The short black lines are inserted lagrangian line segments that are carried by the velocity vector field as time evolves. Their motion further helps visualize the complexities of the resultant vortical flowfield generated by the time-dependent wall jet separation.
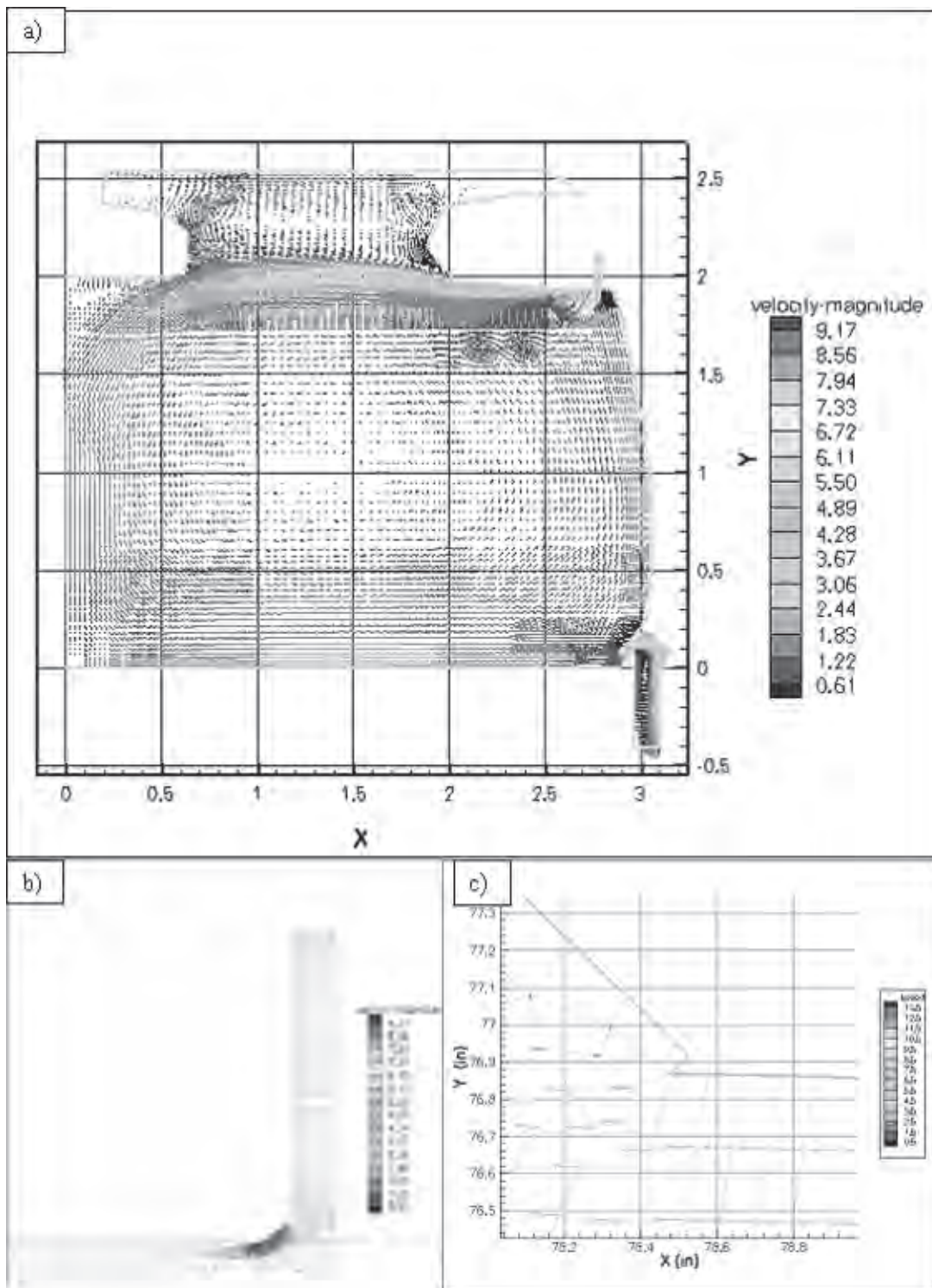
Figure 16. Transverse plane presentation of Fluent generated ventilation velocity vector field in AERF cabin section. Plane Z=108 with both overhead luggage carriers, steady turbulent flow, TKE closure model, a) velocity unit vectors colored by speed, b) magnification of velocity unit vectors in supply plenum-slot jet region, c) mesh modification required for Coanda wall jet separation at luggage carrier terminus. **Legend:** b) Vmag in m/s, c)Speed, ranging from 0.5 –13.5m/s.
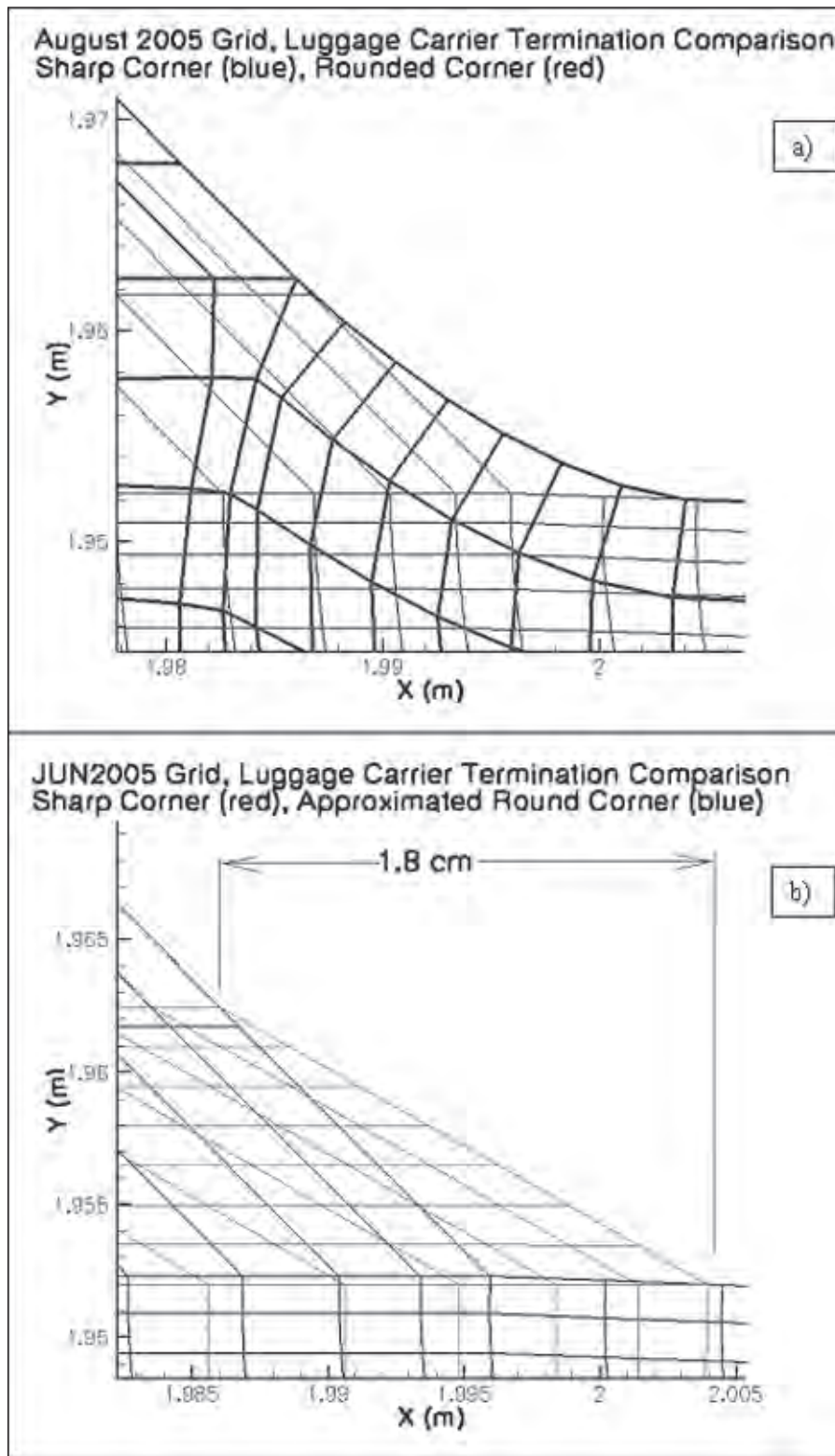
Figure 17. Transverse plane mesh density improvements in luggage carrier terminus region. a) genuine curvature compared to sharp corner approximation, b) tangent approximation to genuine curvature compared to sharp corner approximation.
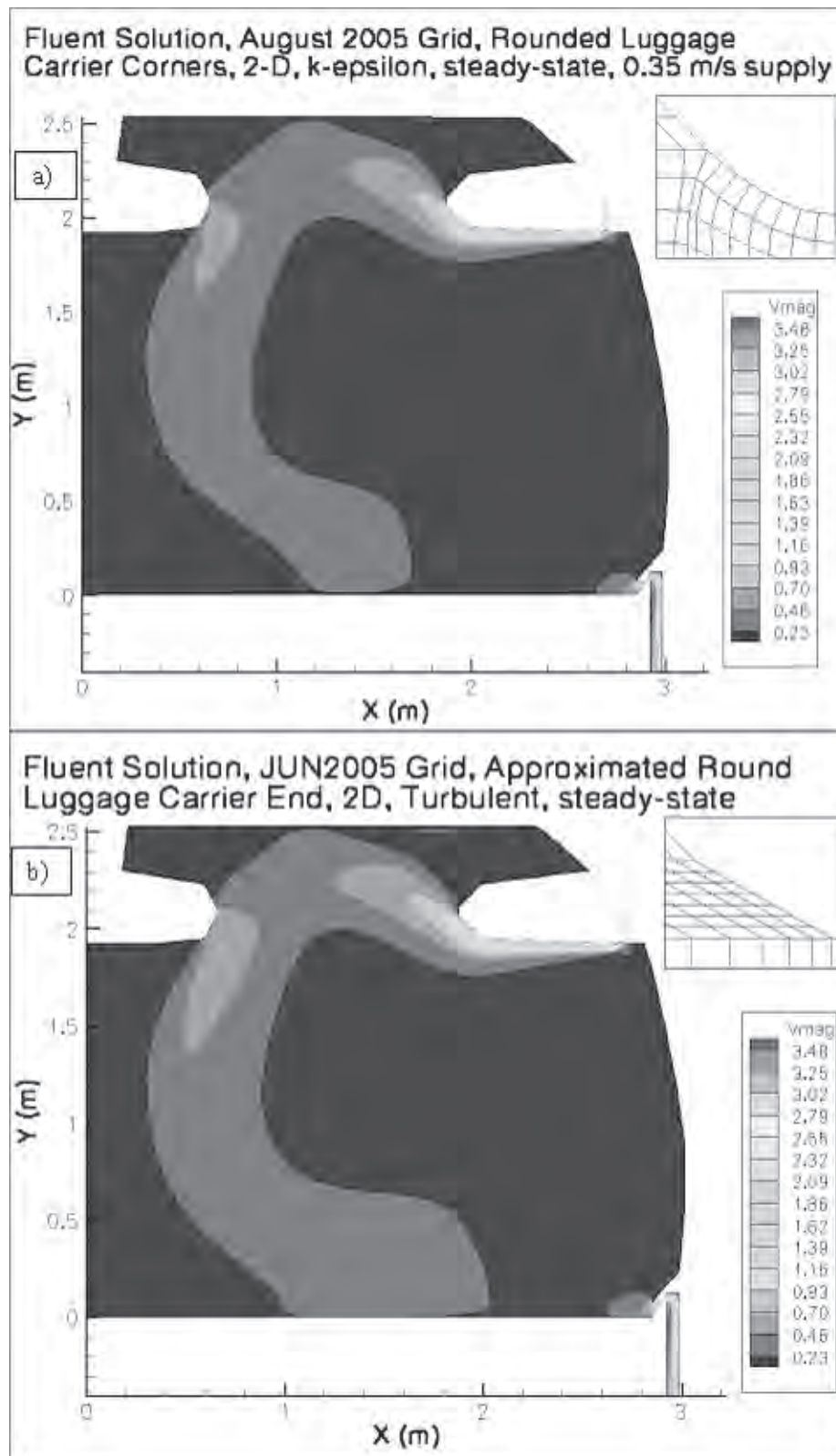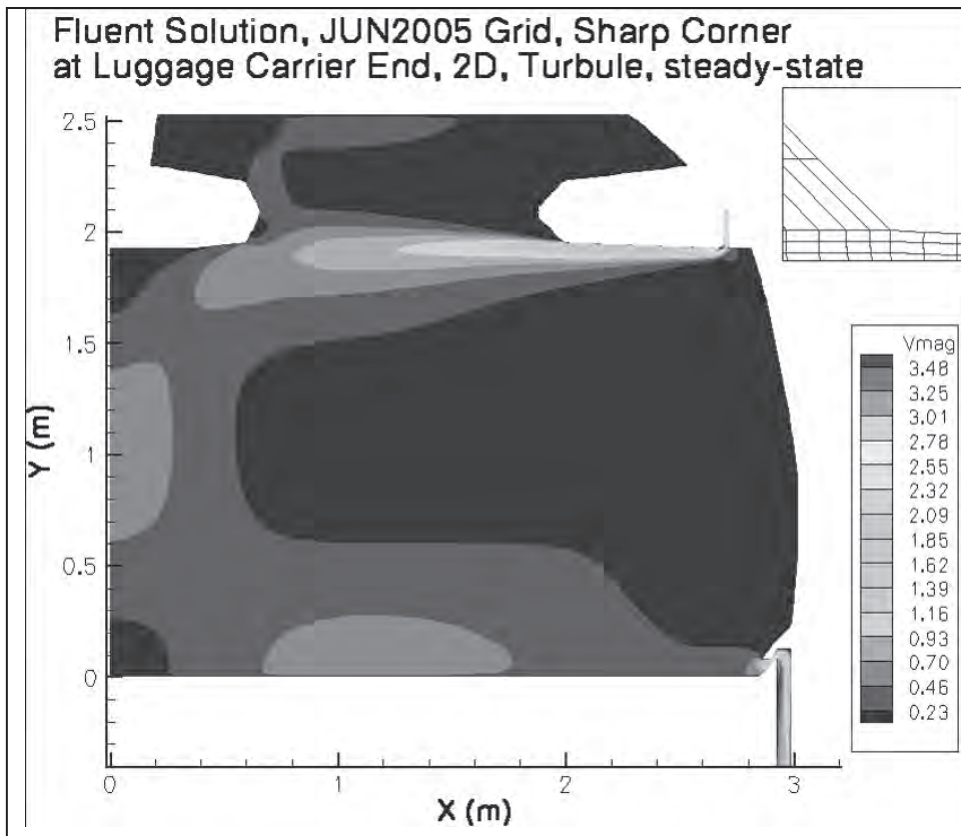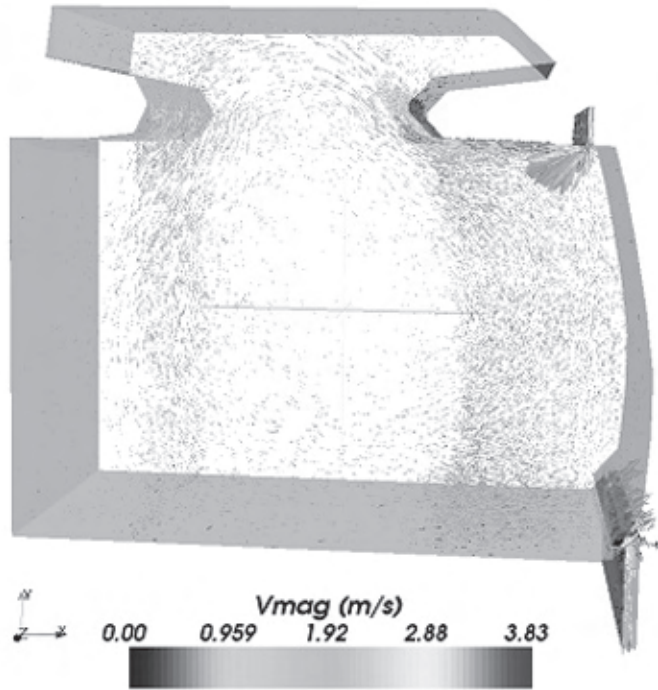
Figure 18. Fluent generated transverse plane circulation patterns, AERF cabin section, plane Z=108 with both overhead luggage carriers, steady turbulent flow, TKE closure model. a) round carrier terminus mesh, b) mesh with tangent approximation to the round carrier terminus. Vmag in m/s.

Figure 19. Fluent generated transverse plane circulation pattern, AERF cabin section, plane Z=108 with both overhead luggage carriers, steady turbulent flow, TKE closure model, mesh with sharp corner approximation to the round carrier terminus. Vmag in m/s.
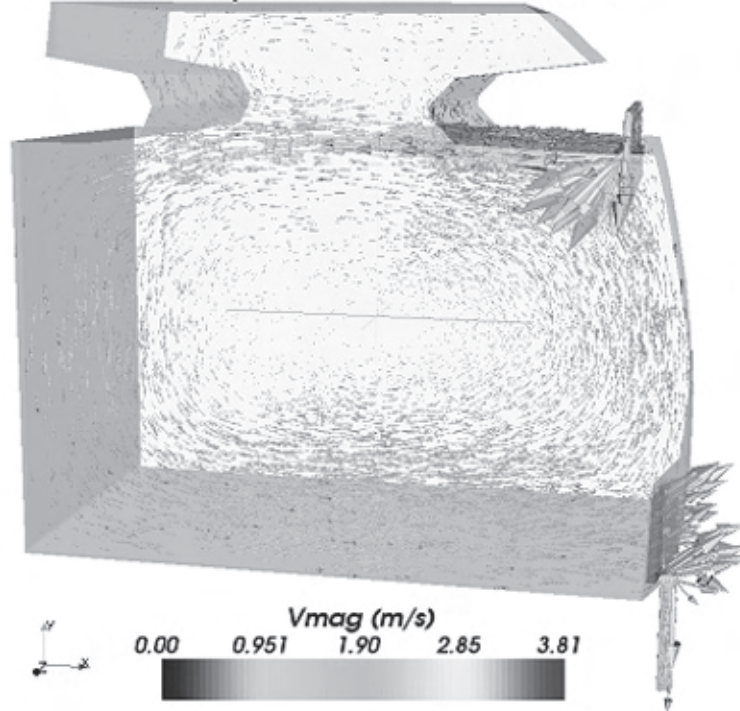
Figure 20. Star CD generated transverse plane circulation patterns, AERF cabin section, plane Z=108 with both overhead luggage carriers, steady turbulent flow, TKE closure model, a) round carrier terminus mesh, b) mesh with sharp corner approximation to the round carrier terminus.
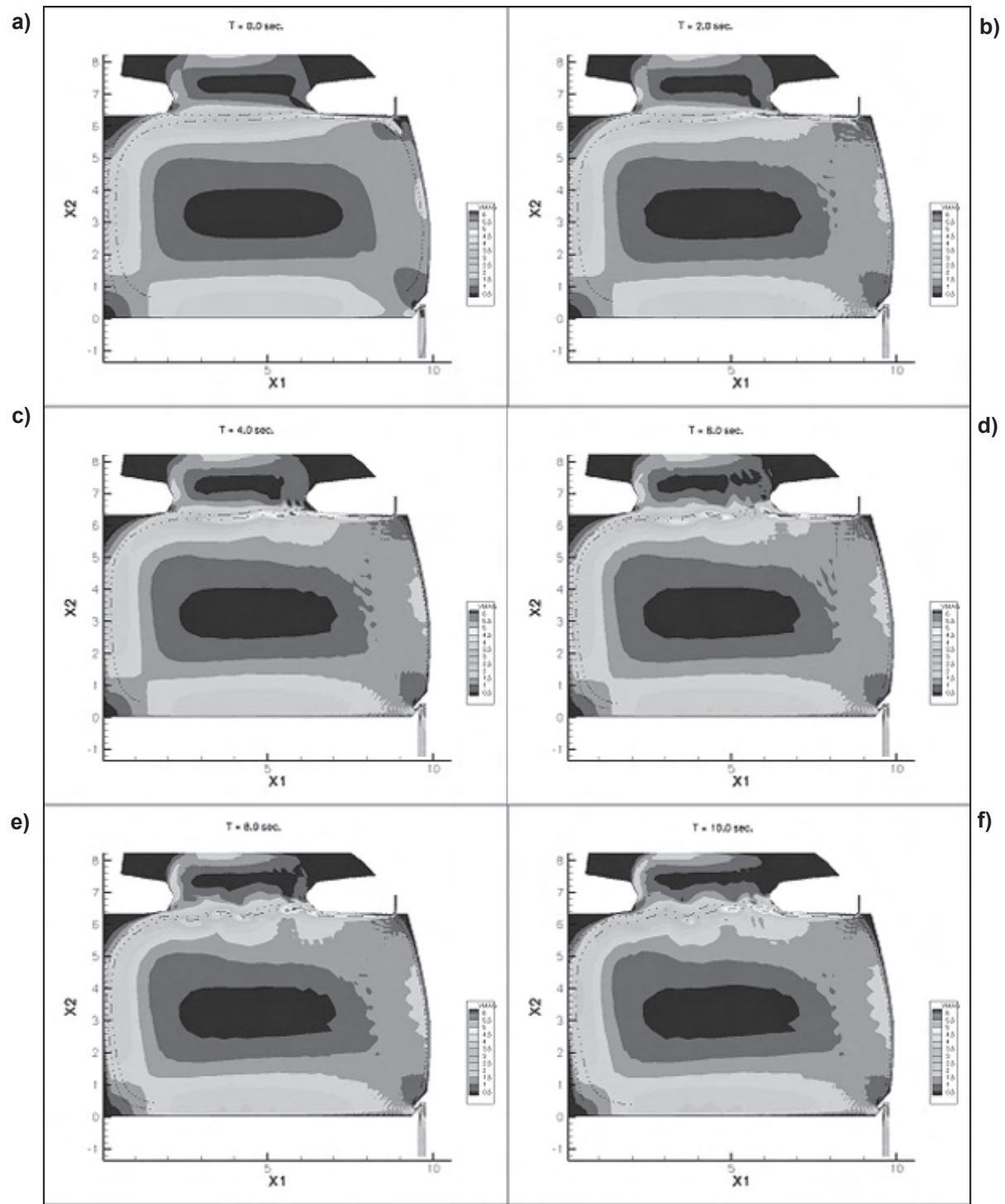
Figure 21. Transverse plane presentation of a PSE generated solution in AERF cabin section, plane Z=108 with both overhead luggage carriers, time-accurate continuation from Fluent steady turbulent flow solution, TKE model, a) t = 0 s, b) t = 2 s, c) t =4 s, d) t = 6 s, e) t = 8 s, f) t = 10 s, g) t = 16 s, h) t = 22 s, i) t = 26 s, j) t = 30 s, k) t = 40 s. **Legend:** Vmag ranging from 0.5 – 6m/s.

26

g)

T = 16.0 sec.

h)

i)

T = 26.0 sec.

j)

T = 30.0 sec.

k)

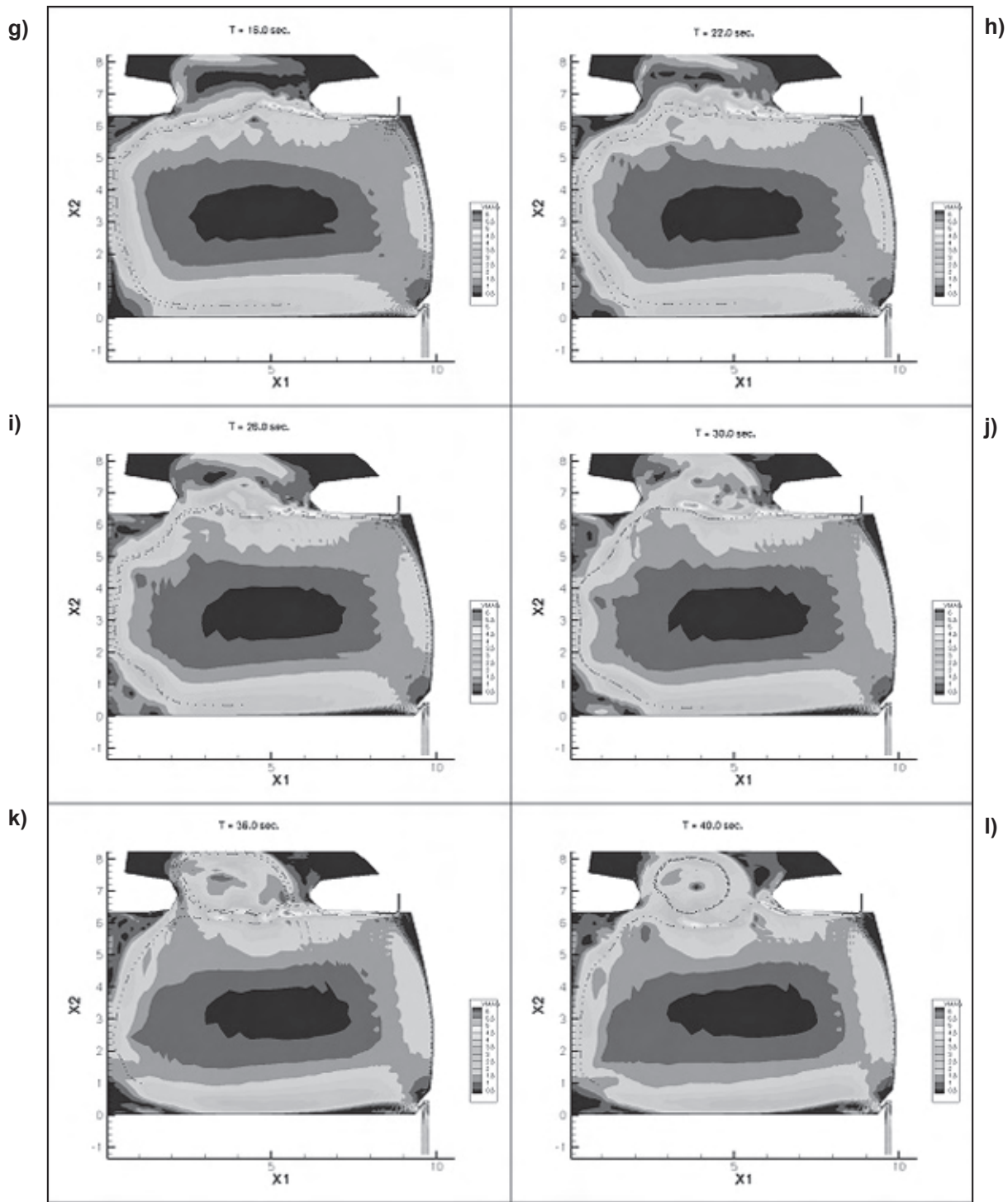T = 36.0 sec.

l)

T = 40.0 sec.

T = 22.0 sec.

Figure 21 (continued).

These CFD data confirm that the inability of the commercial CFD code solutions to correctly predict carrier terminus separation is not due to the TKE log-law BCs. Therefore, one can conclude that this problem stems from the direct steady-state iteration strategy using an inadequate mesh for the sharp corner luggage carrier terminus approximation. The cabin ventilation flowfield is clearly unsteady, as documented by the experimental data and this simulation, with wall jet separation oscillating about some mean as the motive cause. The unsteady CFD simulation further indicates that this unsteadiness penetrates upstream into the wall jet region itself.

This prediction prompted probing of the AERF experimental data to assess the existence of natural frequencies. The 3-s data sample interval significantly compromises assessment fidelity, so it was completed only for the free stream horizontal velocity vector component at the data point closest to the carrier terminus. For the central two min during data recording, Figure 22 graphs the results. The experimental data are the solid symbols, the top curve is the Fourier interpolation, and the middle and bottom curves are the two predicted real frequencies in the interpolation. The resultant periods are the order 15 and 30 s. The time-accurate CFD simulation predicted unsteadiness of the cabin ventilation flowfield is in solid qualitative agreement with this data analysis.

Both commercial codes also state an LES simulation model capability. An LES time-accurate unsteady simulation was initiated using the base code, even though the mesh is not sufficiently refined to admit generation of a genuine LES simulation. The computation was terminated after three weeks' elapsed execution time, which generated solution evolution through 12 s. Figure 23 summarizes the time evolution of the cabin ventilation flowfield graphed as streamlines of the transverse plane velocity field. The solution contains significant vortical content, in firm qualitative agreement with both the experimental data and the research code unsteady TKE simulation.

Baseline cabin mass transport CFD validation exercise

The key step is insertion of the mesh block containing the geometry of the VHP injector, hence quantification of alteration to the base empty cabin velocity field prediction. For the luggage carrier sharp terminus approximation, Figure 24 summarizes these results generated by the base commercial code. Figure 24a) repeats the data of Figure 16a) graphed in the preferred transverse plane contour map colored by speed. Figure 24b) presents the corresponding distribution of turbulence Reynolds number, Re^t, defined as the ratio of TKE model eddy viscosity to the kinematic viscosity of air.
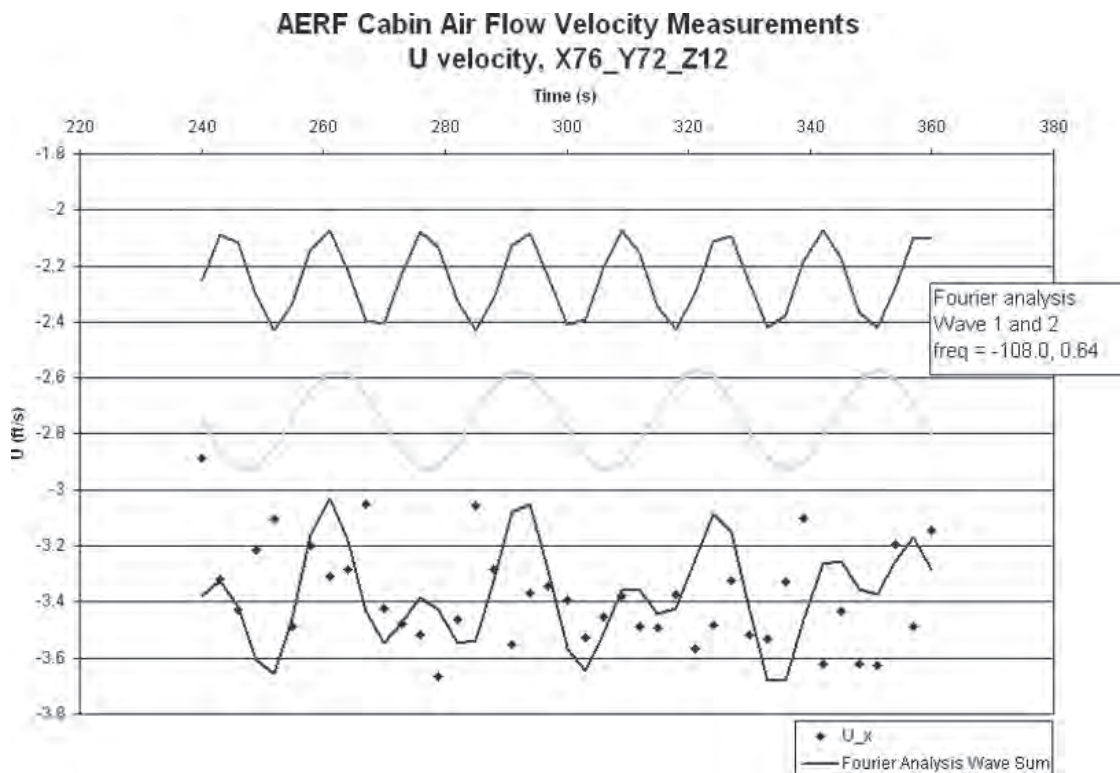

Figure 22. Fourier analysis of AERF experimental data. Cabin section plane Z=108 with both overhead luggage carriers, U_x velocity component, data coordinate closest to the luggage carrier terminus.
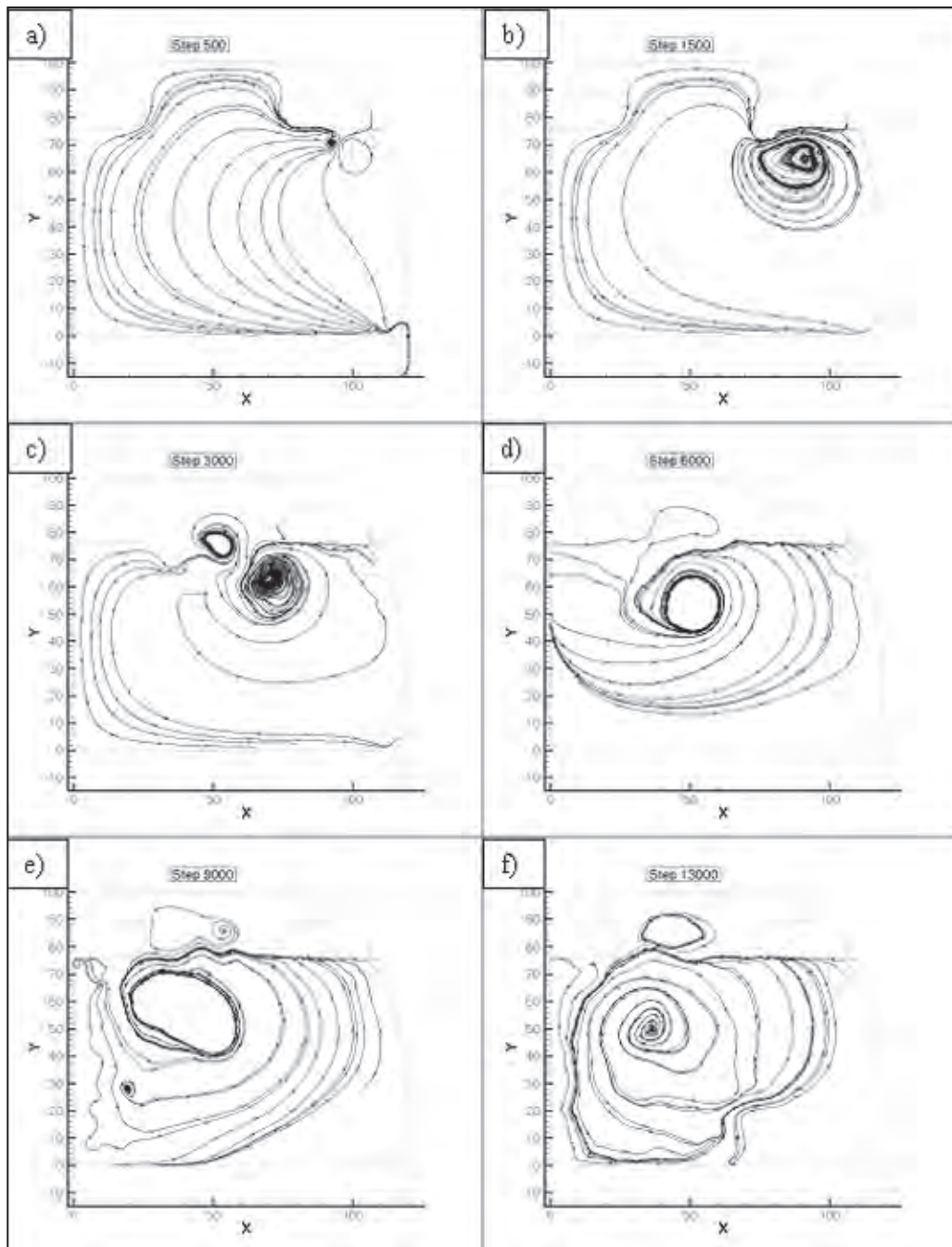
28

Figure 23. Transverse plane presentation of Fluent time accurate solution evolution in AERF cabin section. Plane Z=108 with both overhead luggage carriers, LES closure model, velocity streak lines at various times on 0 < *t* < 12 s.
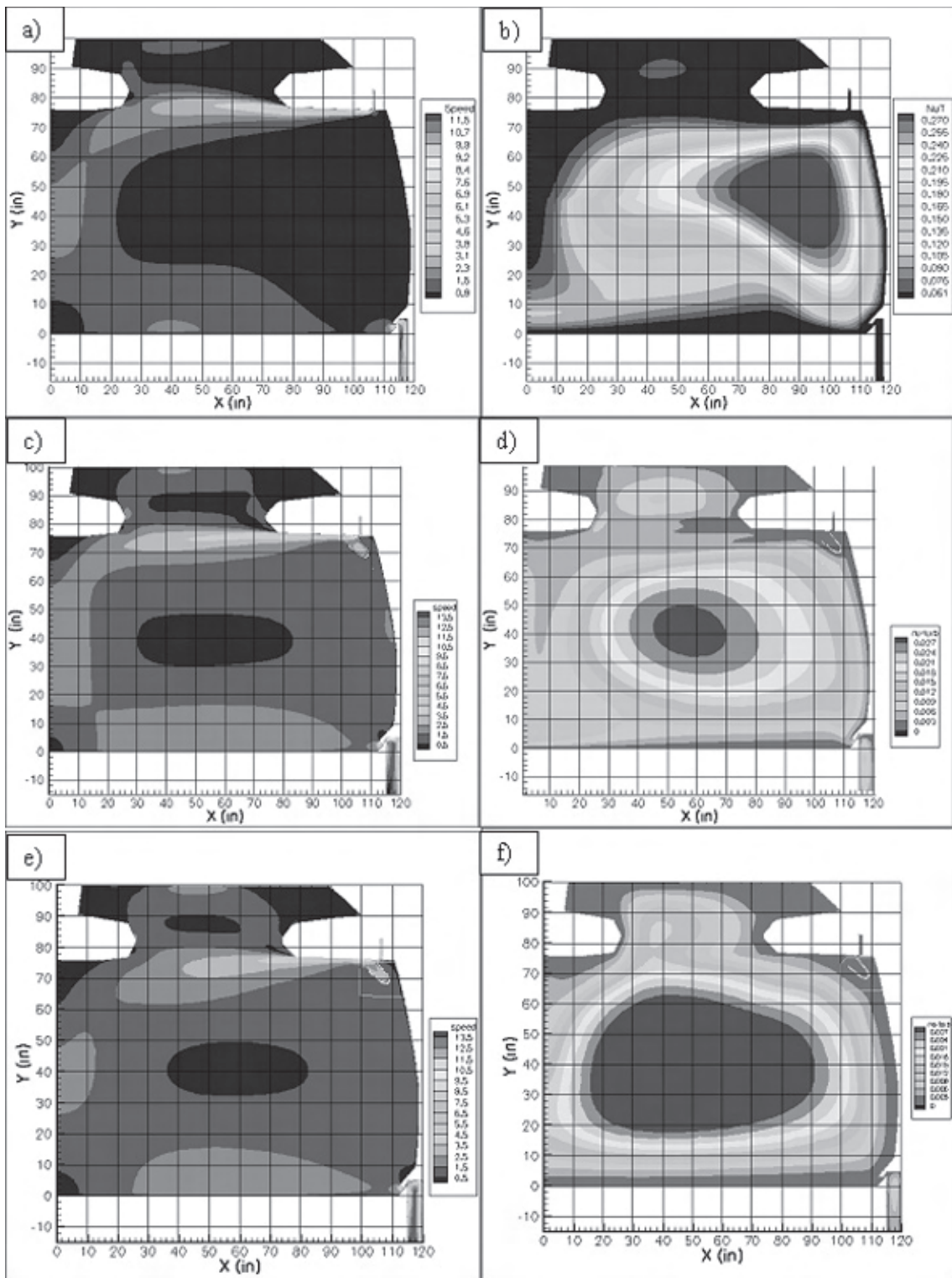
Figure 24. Transverse plane distributions of Fluent generated solution in AERF cabin section. Plane Z=108 with both overhead luggage carriers, steady turbulent flow, TKE model, base mesh, a) velocity magnitude (speed) distribution, b) turbulent Reynolds number Re^t distribution, TKE model; including VHP injector geometry mesh block, c) TKE model velocity magnitude (speed) distribution, d) turbulent eddy viscosity ν^t distribution, e) Spalart-Allmaras model velocity magnitude, f) turbulent eddy viscosity ν^t distribution. **Legend:** a), c), and e) show speed ranging from 0.5 – 13.5m/s; b), d), and f) show NuT ranging from 0 – 0.027.

Figures 24c) – d) present the companion commercial code TKE solution for the domain now including the VHP injector geometry mesh block but with the VHP supply flow set at 2% nominal to prevent backflow. The speed data distribution is sufficiently similar to the base mesh case to provide assurance that the VHP injector geometry would not drastically alter the ECS-generated AERF ventilation flowfield. Figure 24d) graphs the non-normalized (by air kinematic viscosity) TKE eddy viscosity, and a modest visual distinction is apparent.

Also evaluated was base commercial code execution using the Spalart-Allmaras eddy viscosity closure model [21], which produced the steady solution data graphed in Figures 24e) - f). The cabin circulation trajectory identity is less pronounced, i.e., relatively more diffused, which is readily traced to the overall larger level of eddy viscosity generated by this closure model, compare Figures 24d) - f).

All baseline CFD simulations confirmed the AERF cabin ventilation velocity vector field possessed a negligible axial component, even around the central luggage carrier termination. Since the VHP mass injection system was designed to be non-disturbing, with axial span of only 0.1 m (4 in), it was deemed sufficient to employ the standard seat pitch span for the CFD solution domain. Figures 6 - 7 summarize the base geometry and resultant highly non-uniform, mesh-contained 1.2 million nodal points. Vanishing normal derivative BCs for all variables were applied on solution domain faces with unit normal aligned with the cabin axis.

Figure 25 summarizes the commercial code TKE steady solution with the VHP mass injection system operating at nominal setting. The transverse plane speed map, Figure 25a), is visually indistinguishable from the baseline flow computation without mass injection (Figure 16a). The notable distinction is a modest narrowing of both the wall and near field free jet contours due to entrainment of the injectant. The steady distribution of VHP in the cabin axial plane, containing the first experimental sample location (denoted 74,75 in Figure 12), possesses an essential mirror plane of symmetry, Figure 25b). The perspective 3-D presentations of the steady distribution of VHP, Figures 25c)-d), confirm the absence of true symmetry, as induced by the VHP injection system terminus turning the injected flow through a 90° angle.

The key issue with mass transport simulation is time evolution of concentration distributions. In the genuine cabin environment, mass release would occur into the ECS-generated nominal ventilation flowfield. The experimental protocol employed this definition, which was best approximated for CFD experiments by using the cabin flowfield that included the (modest) steady injec-

tion velocity influence. Hence, the only solution process run time accurate was mass transport. The CFD experiment IC was mass fraction initialized within the entire injection piping system and zero everywhere within the cabin. The BCs were mass fraction fixed at the injection system inflow plane and vanishing normal derivative on all other solution domain surfaces.

The baseline CFD simulation was generated using the base commercial code operating time accurate for mass transport within the TKE-model generated steady velocity vector field. Figure 26 graphs the resultant time evolution of predicted mass fraction superimposed onto the experimental data for the four data coordinates closest to the free jet trajectory (recall Figure 12). The coordinate on the abscissa setting the superposition is the time of first appearance of measured and computed non-zero mass fraction, which of course is distinct for each data location.

After extensive analysis, it proved impossible to set with confidence the experimental mass fraction level at the VHP injection face. Therefore, the Figure 26 comparisons are normalized for CFD solution best approaching steady state fit with the experimental data moving average interpolations. Selecting this to occur at sample point (X044-Y072-Z108), Figure 26b) also yielded nominal matching at the sample point furthest from the free jet trajectory, Figure 26d). Consequently, substantial under-prediction of mass fraction level occurs at the closest sample point (X074-Y075-Z108), with over-prediction at the remaining sample point, Figures 26a) and 26c).

The Figure 26 comparisons generate more questions than answers. The CFD predictions obviously do not agree well with the data except at the set point. The severe under-prediction of the CFD level at the closest sample point is particularly concerning, as it could indicate the action of excess numerical or physical (TKE model) diffusion. One significant feature of agreement with this manipulation is the nominal identical slope of both the moving average and CFD solution curves at the time coordinate where VHP was first recorded at each data coordinate.

This observation led to a lagrangian particle transport CFD experiment to estimate the time frame of injectant circulation. Figure 27a) summarizes the time evolution of the coordinates of a lagrangian particle injected into the ventilation supply and VHP injection plenums. Being mass-less, these particles follow exactly the velocity field circulation trajectory into which they are placed.

The key result is that both particles make a complete circulation of the cabin interior within 15 s elapsed time. For the VHP experiment 10-s sampling rate, the longer
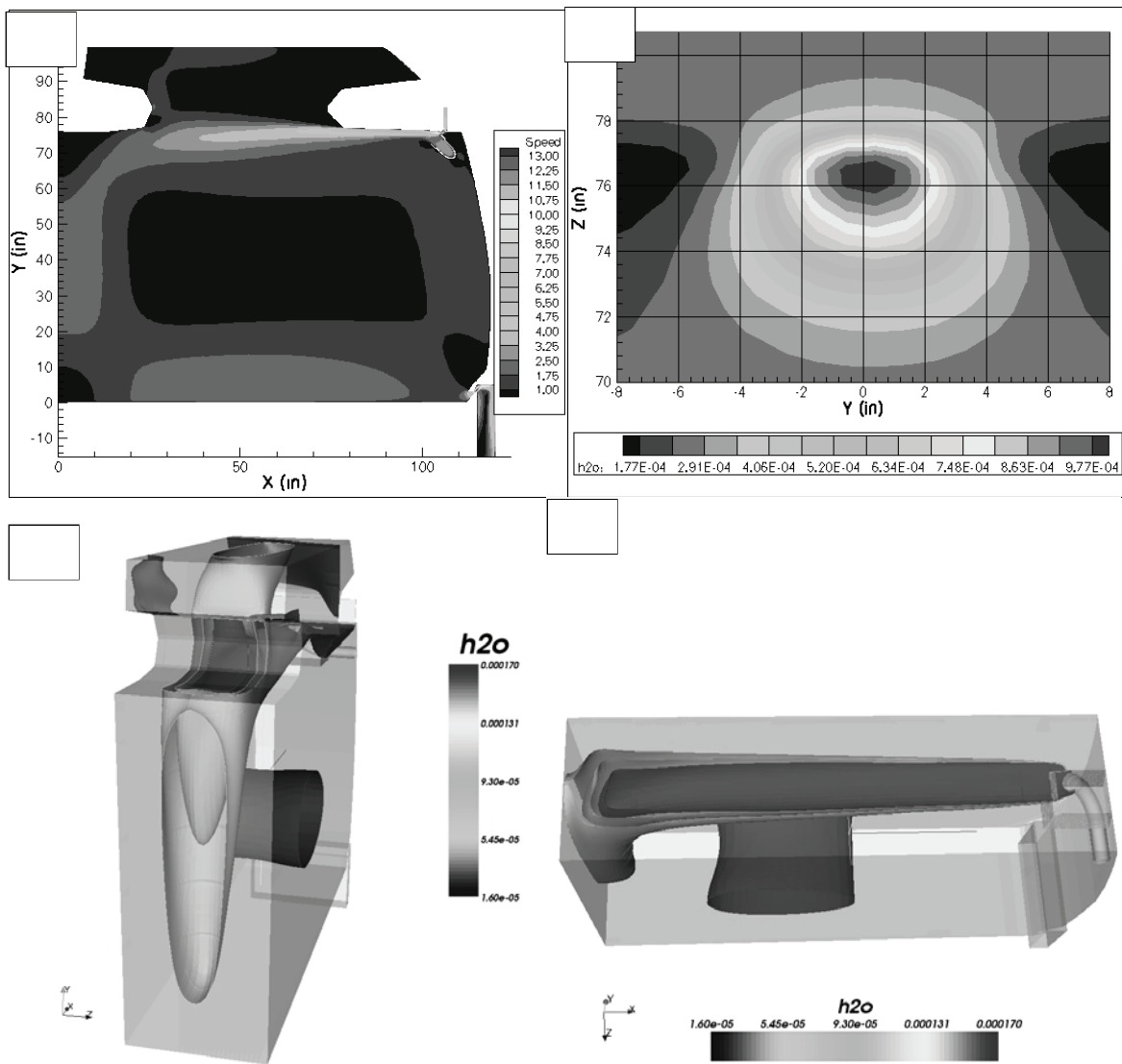
Figure 25. Fluent generated solution in AERF cabin section with VHP injection. Plane Z=108 with both overhead luggage carriers, steady- turbulent flow, TKE model, a) transverse plane velocity magnitude (speed) distribution, b) lateral plane mass fraction distribution containing sample point X=074, Y=075, c) 3-D perspective view of mass fraction distribution looking towards injector, d) 3-D perspective view of mass fraction looking down.

Figure 26. Fluent generated solution for VHP time histories comparison with experimental data at four sampling coordinates, steady turbulent flow, TKE model, a) X074-Y075-Z108, b) X044-Y072-Z108, c) X028-Y072-Z108, d) X034-Y064-Z108.
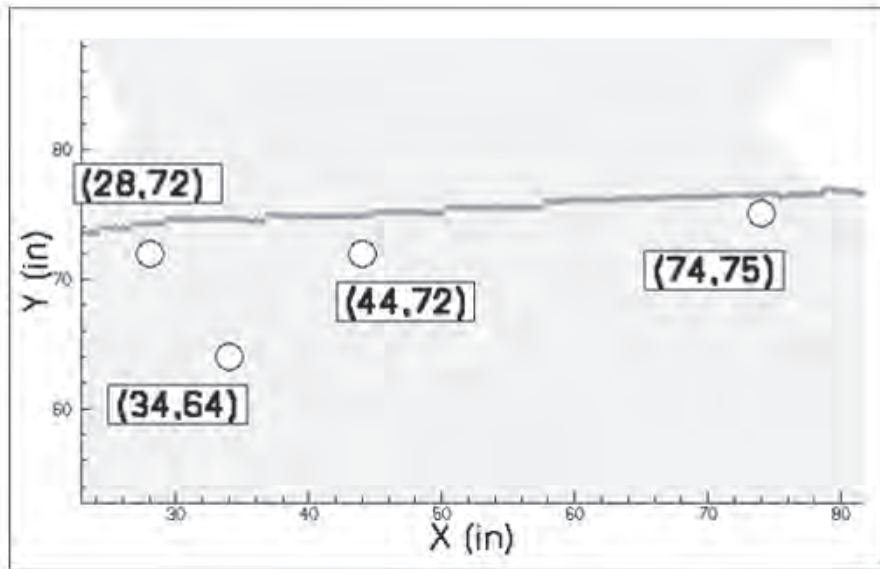
33
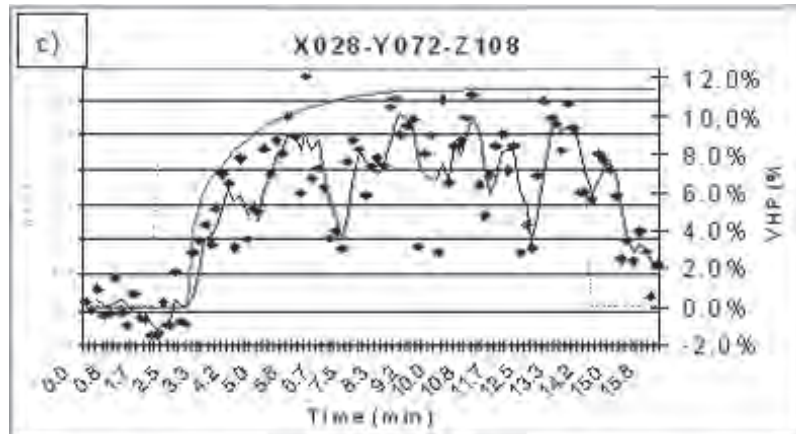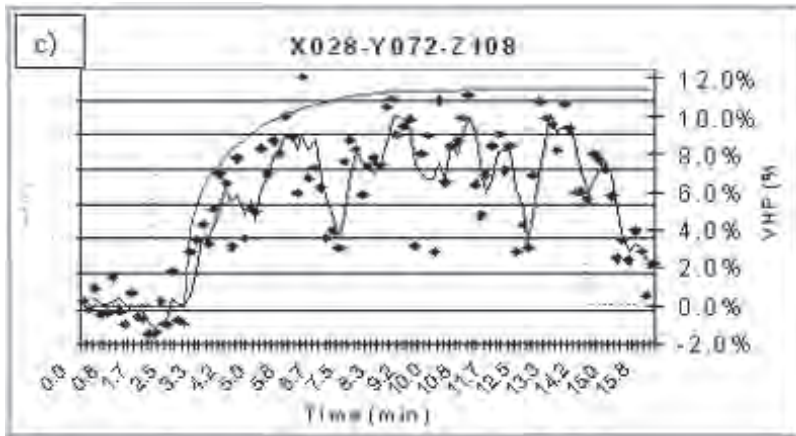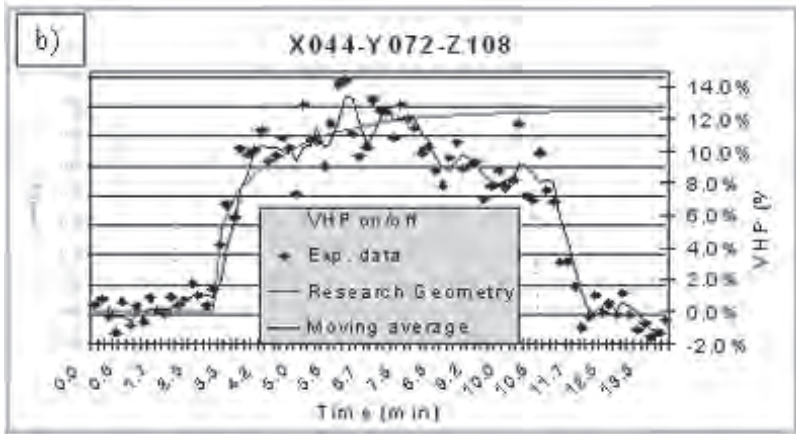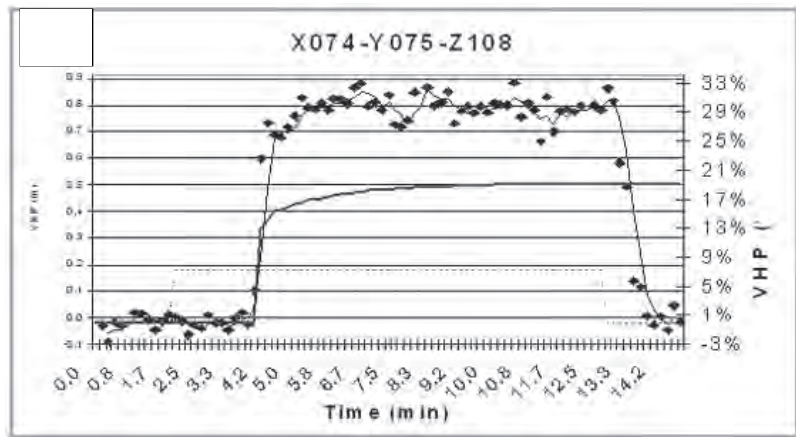
a)
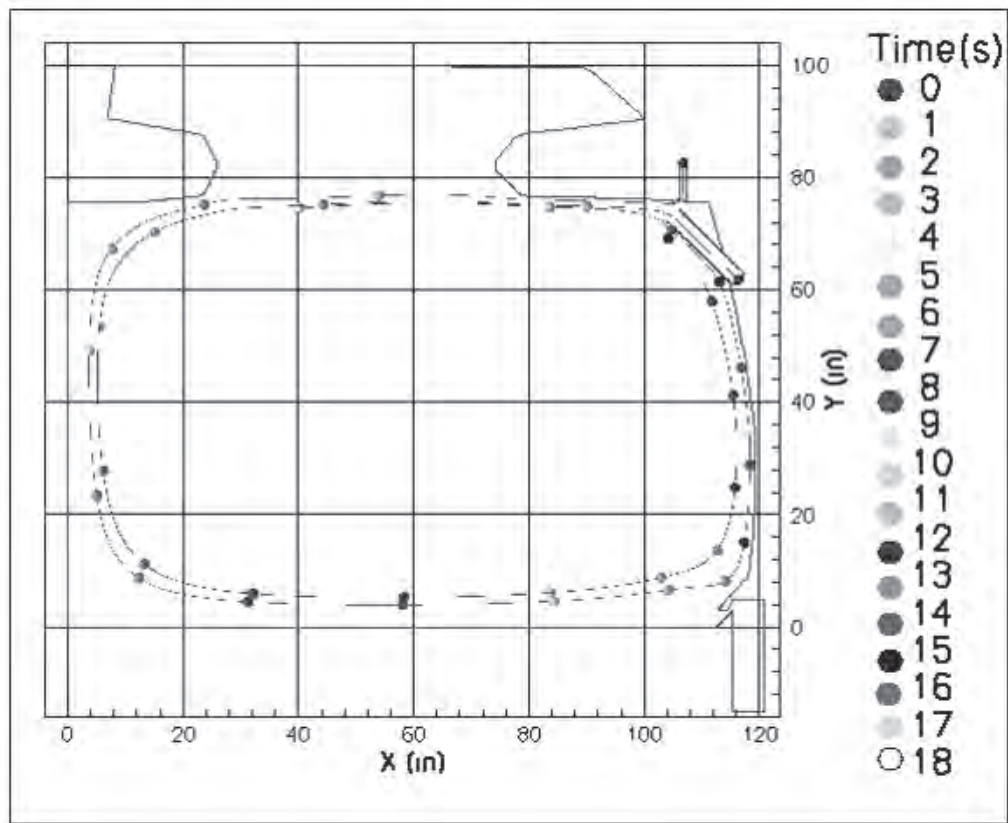
b)

Figure 27. Computed time history of VHP penetration and circulation in AERF cabin. a) Lagrangian particle track evolution for particles injected into ventilation supply and VHP supply, b) computed maximum mass fraction trajectory compared to experimental sample points.

time data really record accumulation of VHP after multiple cabin circulations, hence accumulation. Thereby, the sole reliable data samples for VHP time-evolution assessment are only those acquired in the first 15 s of an experiment. Further, the viable data sample locations are only those discussed, the locations of which are compared to the CFD predicted trajectory of maximum VHP in Figure 27b).

Mass transport fidelity CFD experiments

From the baseline mass transport assessment of VHP experimental data reliability, a sequence of CFD experiments were designed, conducted, and coded to add insight to CFD use issues that might facilitate extracting value from these data. Since the production research code cannot handle mixed tetrahedron-hexahedron meshes, a modification to the mass injection piping system (Figure 7a) was made that enabled simulation using a purely hexahedron mesh. Thereby, the VHP circular piping system was replaced with a straight section of rectangular tubing that would have penetrated the cabin sidewall if actually installed in the AERF.

Figures 28a)-b) present perspective mesh blocks views of this modification, which not only eliminated the need for tetrahedron meshing but also enabled injectant BC application at a distance sufficient to develop a fully turbulent velocity field before entering the cabin. The axial span of the solution domain remained identical to the genuine geometry case, the local meshing remained highly non-uniform (Figure 28c-d), and the resultant domain mesh contained 952,041 nodes.

The base commercial code with TKE closure model was executed on the revised problem geometry, producing a steady velocity field solution in a matter of hours. Visually, the resultant velocity and turbulent viscosity fields were essentially identical to those of the genuine geometry solution, compare Figures 29a)–b). The resultant steady mass fraction transverse plane distributions were also visually essentially identical. For a symmetry plane passed through the terminus of the genuine and modified injector geometries (Figures 29c–d) confirm the computed mass fraction distributions at 20 s elapsed time into the simulation are, for the present purpose, indistinguishable.

With this assurance of simulation essential similarity, the commercial code steady velocity and turbulence fields were ported to the production research code. A matrix of computational experiments was executed to precisely assess the impact of TKE turbulence closure model *and* numerical dissipation mechanisms on time evolution of mass fraction distributions. Figure 30 compares research code predictions of symmetry plane mass fraction distri-

butions, after 20 s elapsed time, for zero turbulent and numerical viscosity, and input constant laminar flow binary diffusion coefficients of d = 0.64E-04 m^2/s (1.0 in^2/s) and d = 0.64E-03 m^2/s (10.0 in^2/s). These selections for d generate solutions that under-predict and over-predict, respectively, the transverse plane diffusion of the mass fraction plume compared to the base commercial code TKE execution (Figure 29d).

Thereby, the input constant binary diffusion coefficient d = 0.29E-03 m^2/s (4.0 in^2/s) produces a mass fraction solution, the penetration and lateral diffusion of which exhibits quite close agreement with the base commercial code TKE solution at t = 20 s, compare Figures 31a) and 29d). Adding the TKE solution turbulent viscosity distribution to this input constant generates the mass fraction solution at t = 20 s (Figure 31b). Focusing on the light blue, different contours, the penetration of the plume is nominally halved, due to the TKE model-induced added level of diffusion.

The subsequent CFD experiment tests the action of numerical diffusion on plume penetration, retaining use of the commercial code TKE simulation steady velocity field. An unsteady mass fraction simulation was executed using this code with its third-order numerical dissipation mechanism, the TKE diffusion term shut off and specifying the unrealistically small laminar binary diffusion coefficient d = 0.29E-05 m^2/s (0.04 in^2/s). The same data specification was executed using the prototype production research code with its numerical dissipation option turned off. Figure 32 compares the generated mass fraction distributions at t = 20 s, which clearly confirms that excessive numerical diffusion exerts a dominating influence on unsteady mass transport prediction fidelity.

The final CFD experiment tested the influence of time integration truncation error on baseline mass fraction solution. All solutions discussed to this point employed a time-step of Δt=0.1 s using the implicit, second-order accurate non-dissipative trapezoidal rule integration algorithm. The production research code simulation for zero TKE diffusion and input constant binary diffusion coefficient d = 0.17E-03 m^2/s (2.5 in^2/s) was repeated using Δt=0.05 s. Figures 33a)-b) graphically compare solution differences globally and locally about the VHP injection tube terminus. These data confirm that the truncation error associated with use of the standard time-step size is a negligible influence on the mass fraction solution everywhere except immediate to the injection tube terminus. Of note, the Courant number (non-dimensional time step) for the Δt = 0.1 s solution ranges from C = 9.6 at the VHP injector to C = 90 at the ventilation supply slot.
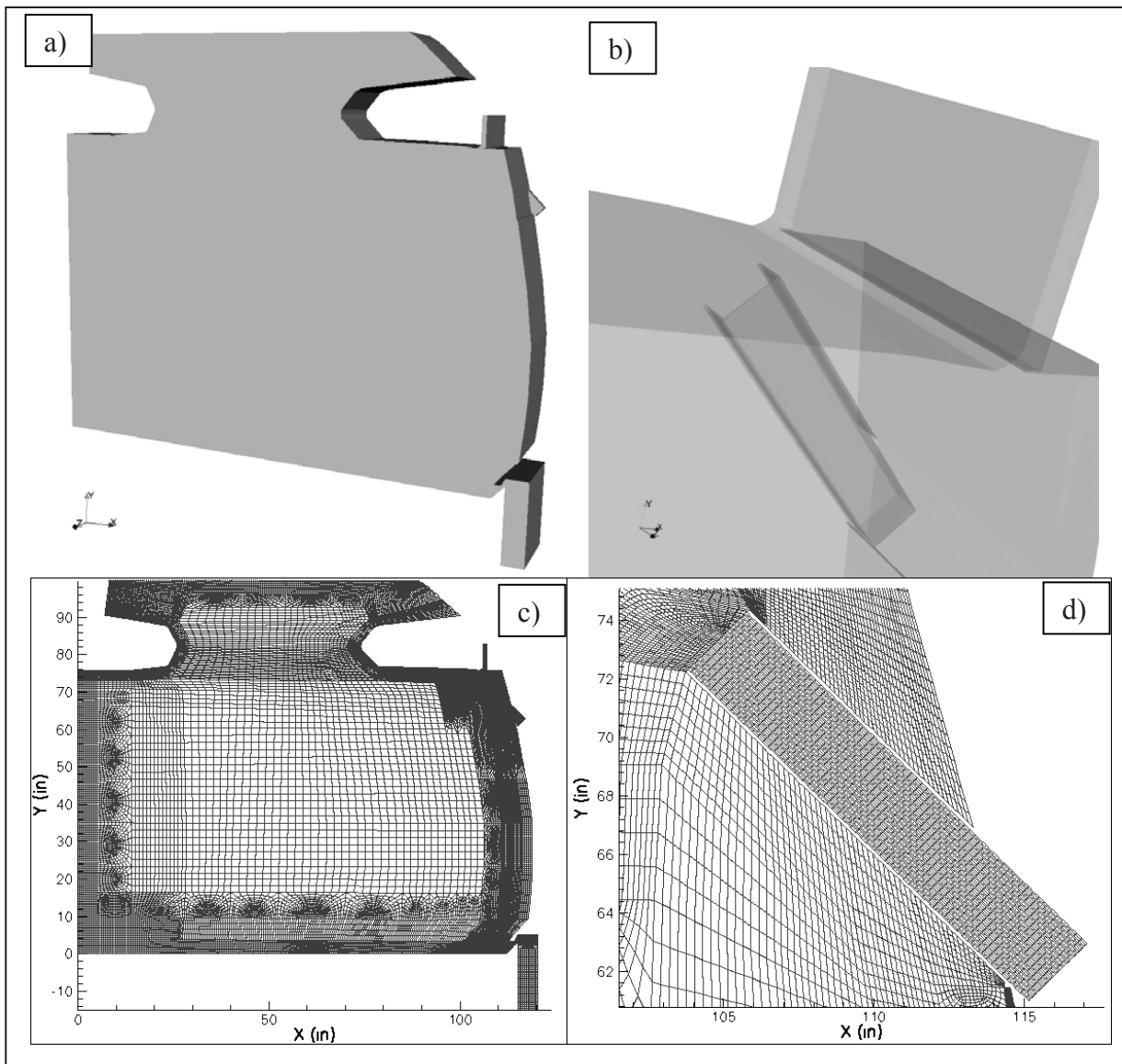
Figure 28. Generated computational mesh of purely hexahedron-shaped cells for a segment of the AERF cabin without seat rows, VHP injection modified geometry. a) perspective view illustrating mesh block geometric essence, b) planar cross-section showing solution-adapted non-uniform meshing for local field resolution, c) modified VHP injection geometry mesh block, d) magnification of VHP injector local region meshing.
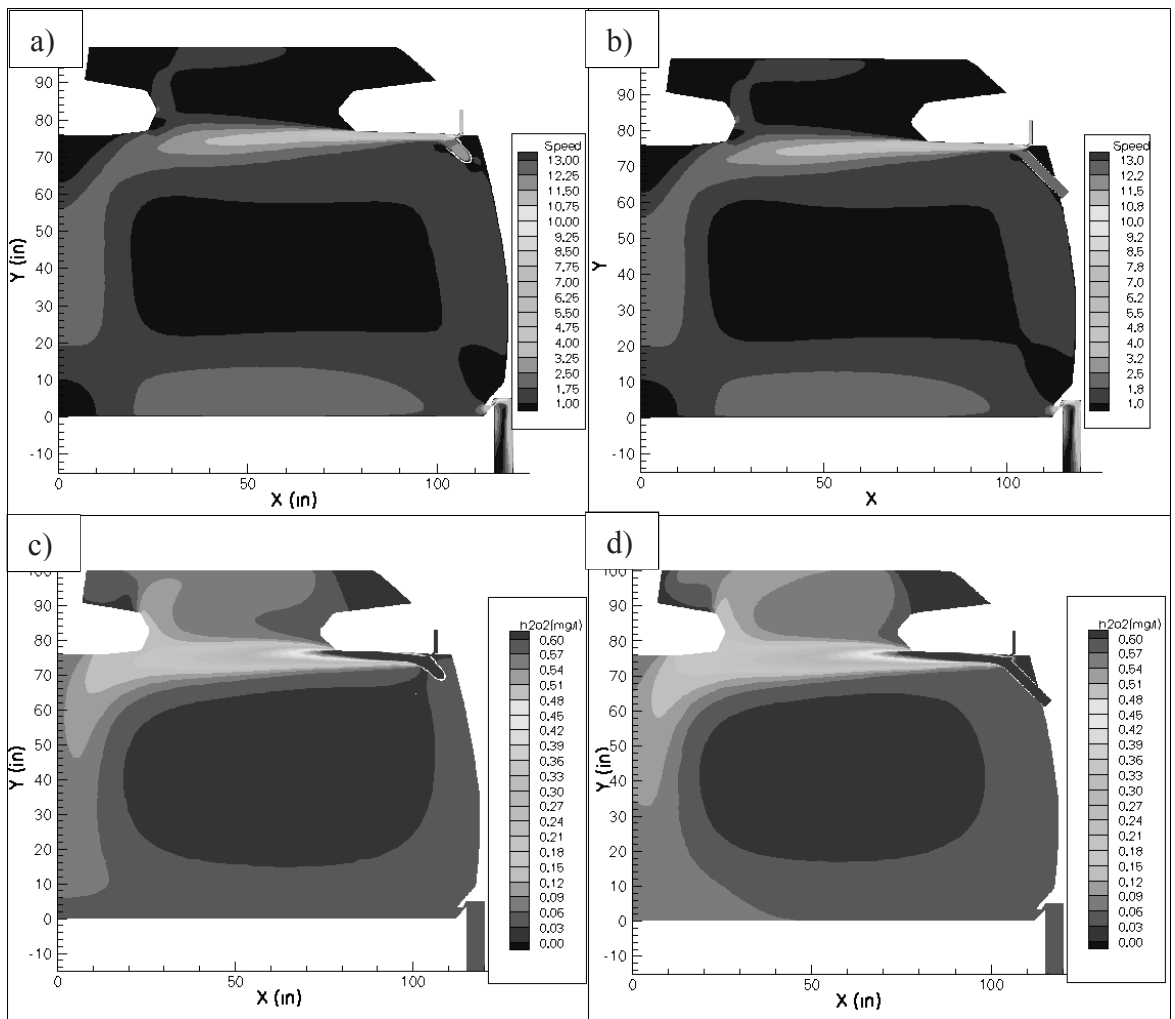
Figure 29. Transverse plane presentation of Fluent generated solution in AERF cabin section with VHP injection, plane Z=108 with both overhead luggage carriers, steady turbulent flow. a) genuine injector geometry, b) modified injector geometry, c) genuine geometry mass fraction distribution at t = 20 s, d) modified geometry mass fraction distribution at t = 20 s.
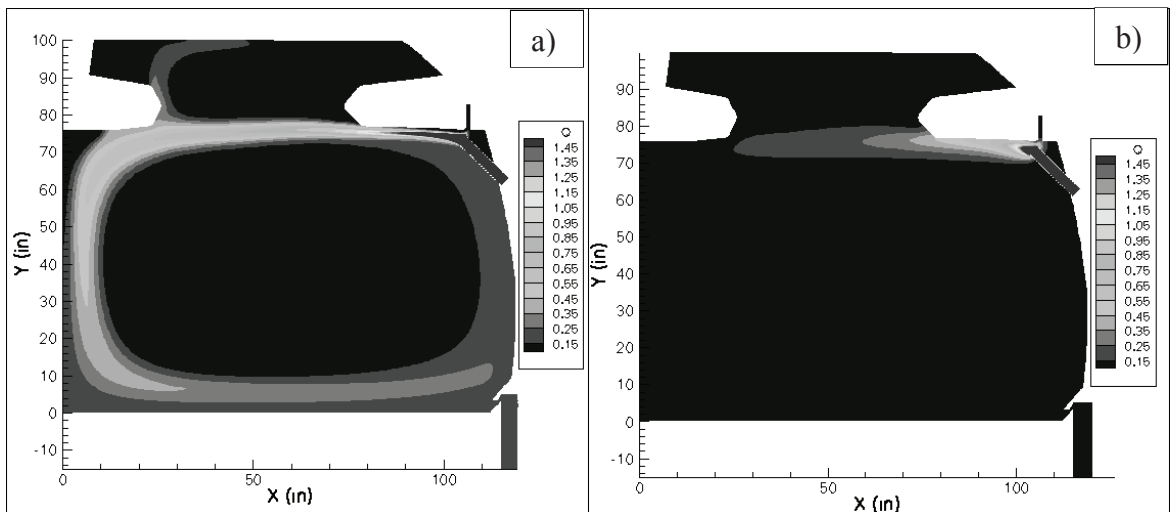

Figure 30. Transverse plane presentations of PICMSS generated VHP distributions in AERF cabin section, Z=108, modified geometry, steady TKE turbulent velocity field, t = 20 s, for constant mass binary diffusion coefficient. a) d = 1.0 in^2/s, b) d = 10.0 in^2/s.
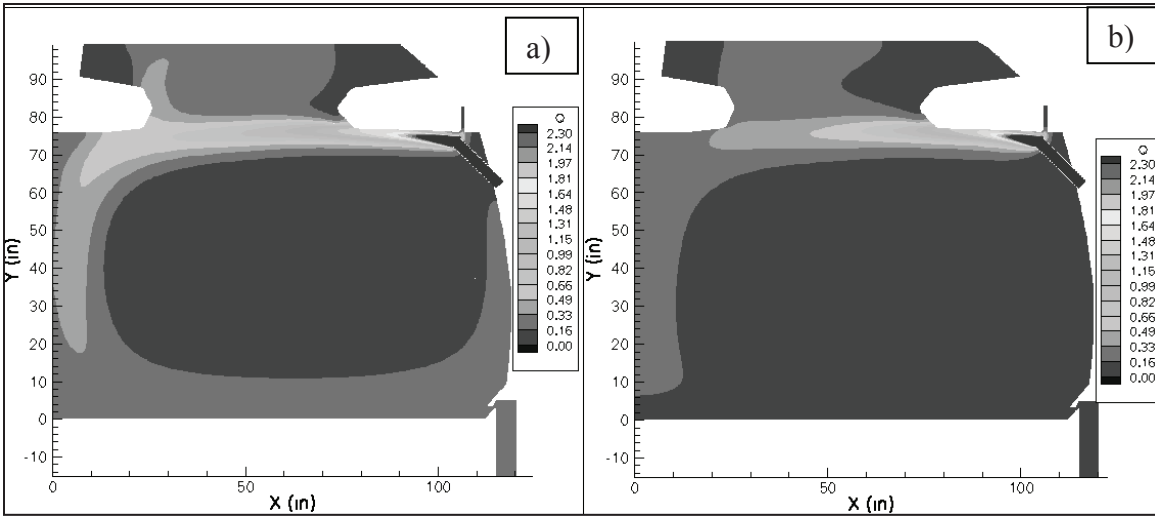
Figure 31. Transverse plane presentations of PICMSS generated VHP distributions in AERF cabin section, Z=108, modified geometry, steady TKE turbulent velocity field, t = 20 s, constant mass binary diffusion coefficient d = 4.0 in^2/s. a) without TKE solution turbulent diffusion coefficient distribution, b) with TKE solution turbulent diffusion coefficient distribution.
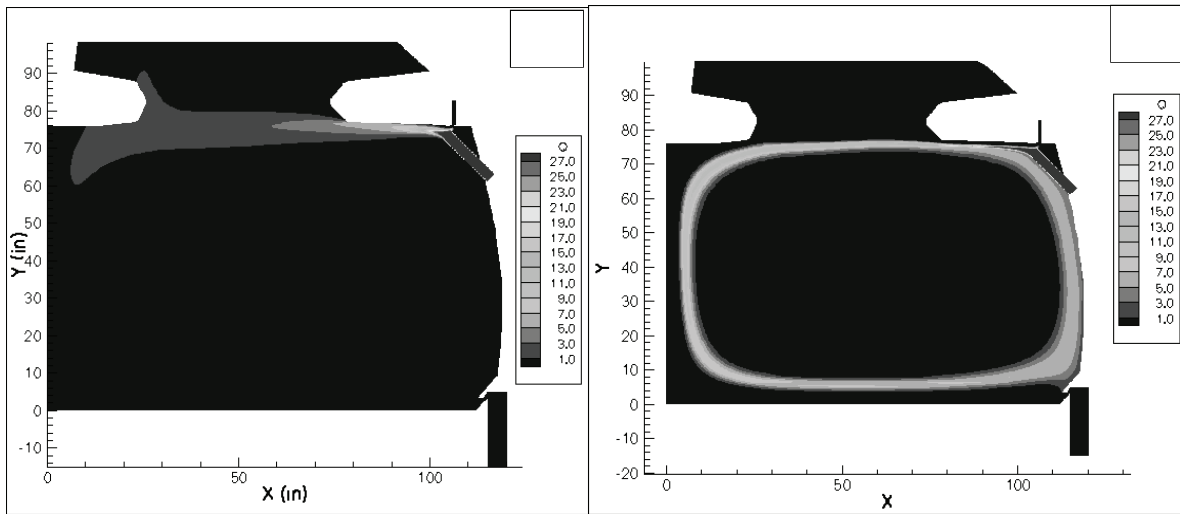

Figure 32. Transverse plane presentations of CFD algorithm generated VHP distributions in AERF cabin section, Z=108, modified geometry, steady turbulent velocity field, t = 20 s, constant mass binary diffusion coefficient d = 0.04 in^2/s. a) Fluent solution with numerical diffusion, b) PICMSS solution without numerical diffusion.
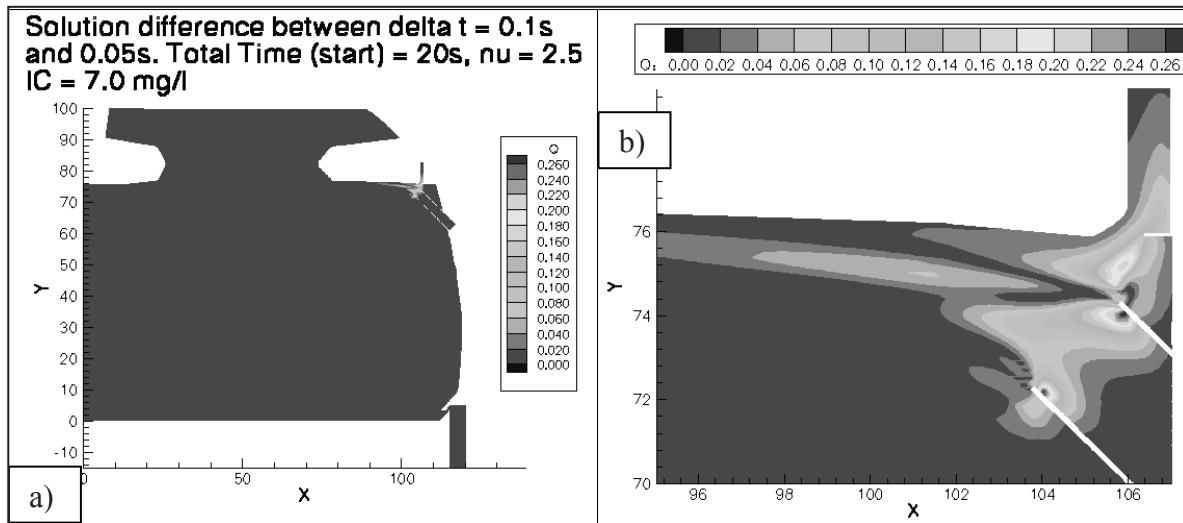

Figure 33. Integration time step error assessment, PICMSS generated VHP mass transport in AERF cabin section, Z=108, modified geometry, steady turbulent velocity field, t = 20 s, constant mass binary diffusion coefficient d = 2.5 in^2/s. a) difference in 2 solutions on transverse plane, b) local magnification near VHP injection.

38

VHP temporal evolution CFD prediction

With an incisive understanding of the VHP injection experiment thus established, a set of CFD experiments sought to accurately quantify controlling aspects of the time-dependent simulation of VHP injectant distributions. Using the modified injection geometry mesh, the production research code was executed for a range of diffusion level specifications. The input steady velocity field remained that was generated by the base commercial code TKE solution, but the TKE eddy viscosity distribution was not used. The experiments employed the non-diffusive trapezoidal rule time integration algorithm, a zero level of numerical diffusion and input values for d, the laminar binary diffusion coefficient.

Figure 34 graphs the production research code computed time-evolution of VHP mass fraction at each of the four experimental sample points lying close to the path of the ventilation free jet (recall Figure 12, for d = 0.29E-03 m^2/s [4.0 in^2/s]). The time delay in appearance of VHP at each location is precisely indicated, as is the onset of VHP accumulation due to complete circulation around the cabin half-span. From these data, it is clear that the injectant front passes these first four sample points within 4 s elapsed time. Figure 35 graphs the t = 20 s z-axis distributions of VHP lateral spread at each of the four sample coordinates, just prior to circulation-induced VHP addition at the first sample point. Each of these contours exhibits the expected Gaussian distribution.
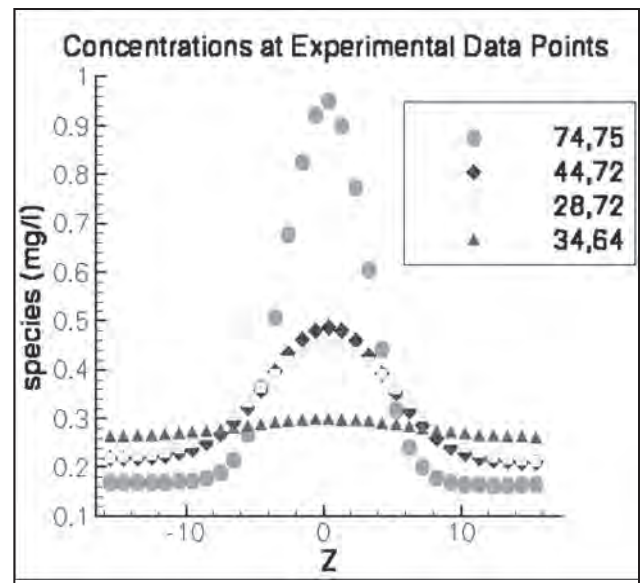

Figure 35. Lateral direction VHP mass fraction distributions at 4 experimental data coordinates, PICMSS time-accurate mass transport solution in AERF cabin section, Z=108, modified geometry, steady turbulent velocity field, constant binary diffusion coefficient d = 4.0 in^2/s, t = 20 s.

Figure 36 summarizes the comparative results of the range of CFD experiments predicting time evolution of the VHP mass fraction level at the four prime experimental data points. These data are normalized to match the first non-zero experimental value at the third sample point (028,072,108) (recall Figures 12 & 26). The three experimental data symbols on each graph are the zero
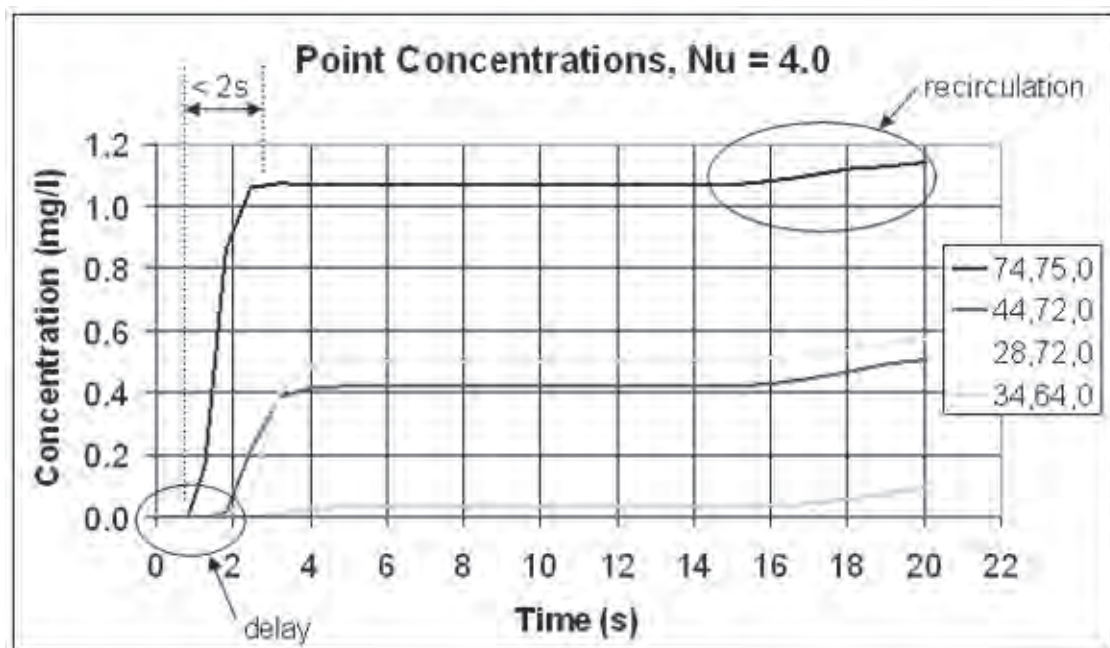

Figure 34. Time evolution of VHP mass fraction at 4 experimental data coordinates, PICMSS time-accurate mass transport solution in AERF cabin section, Z=108, modified geometry, steady turbulent velocity field, constant binary diffusion coefficient d = 4.0 in^2/s, 0 < t < 20 s.

Figure 36. Comparison of time evolution of VHP mass fraction levels to data at 4 experimental data coordinates, PICMSS and Fluent time-accurate mass transport solutions in AERF cabin section, modified geometry, steady turbulent velocity field, TKE and various constant binary diffusion coefficients, data matched at coordinate (028, 072, 108), $0 < t < 20$ s.
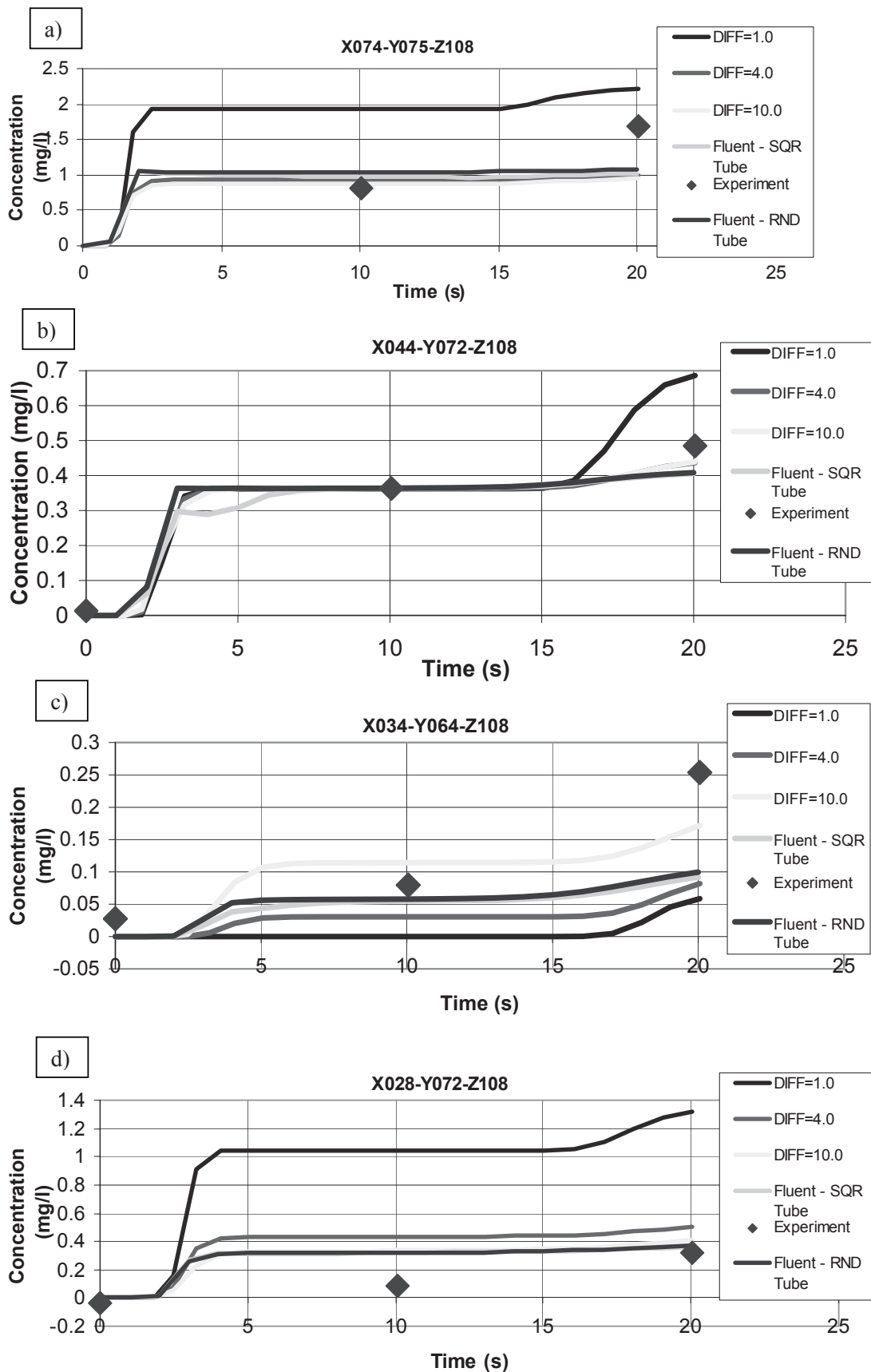
40
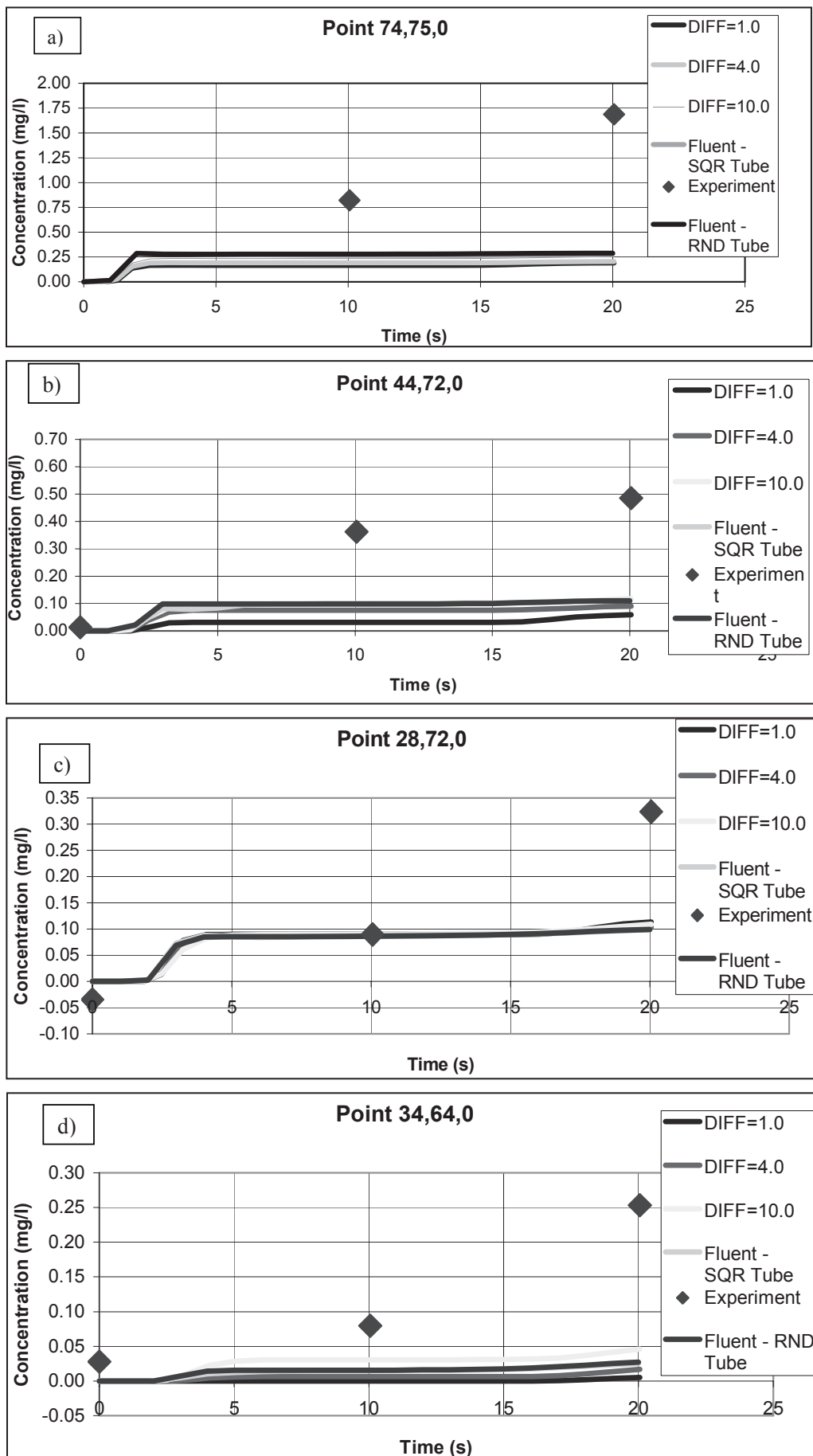
Figure 37. Comparison of time evolution of VHP mass fraction levels to data at 4 experimental data coordinates, PICMSS and Fluent time-accurate mass transport solutions in AERF cabin section, modified geometry, steady turbulent velocity field, TKE and various constant binary diffusion coefficients, data matched at coordinate (044, 072, 108), 0 < *t* < 20 s.
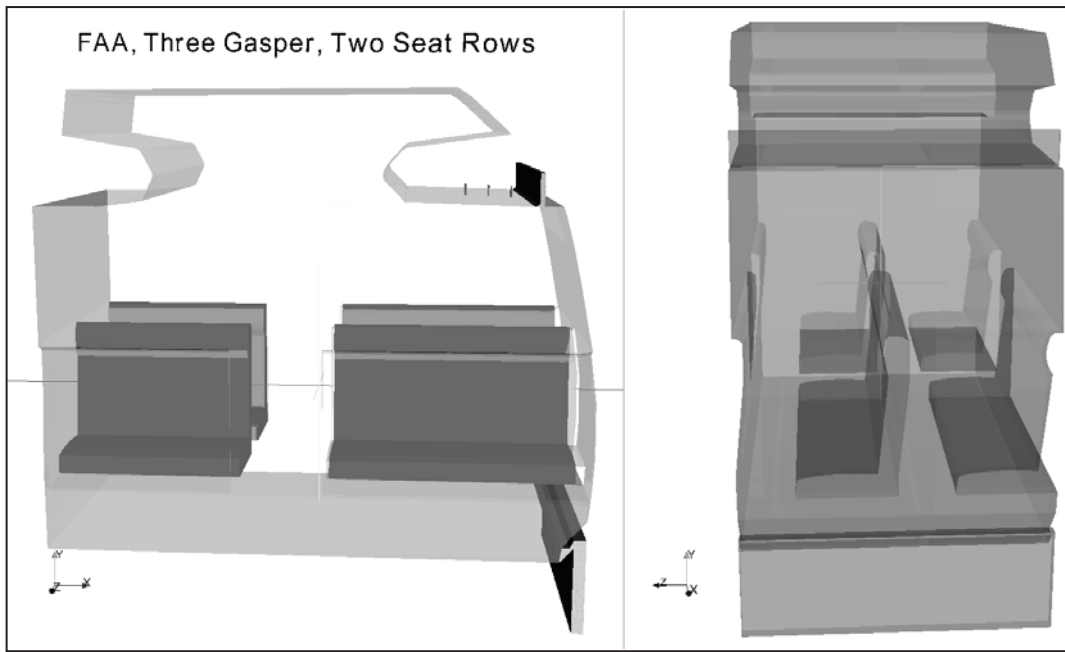
Figure 38. Solution domain for CFD simulation of ventilation flow in the fully configured AERF cabin. a) (left) axial view of the half-span double seat row solution domain block with gasper, supply and exhaust plenums fully visible, b) transverse view showing axial span mesh block termination transects on seat backs.
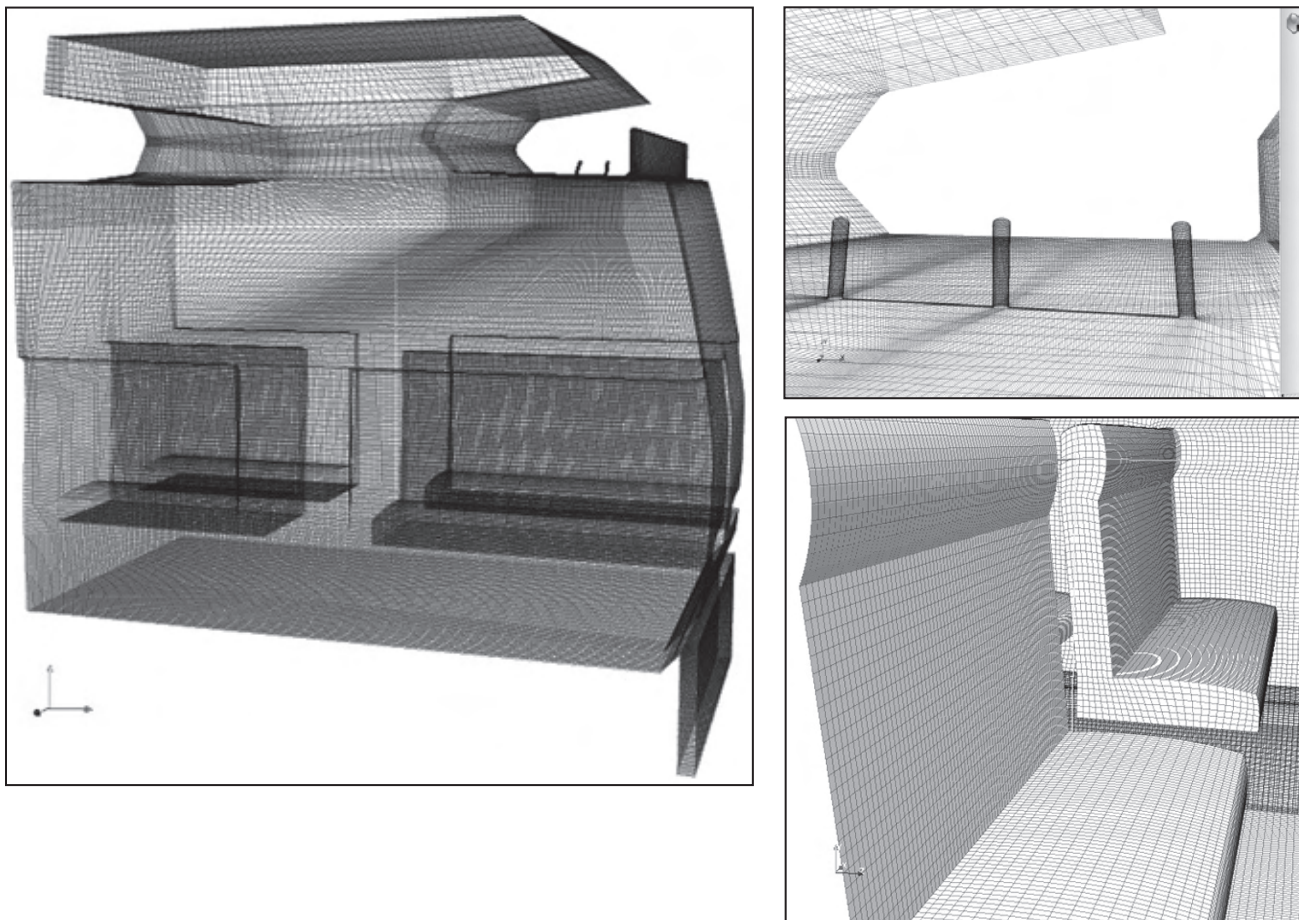
Figure 39. Computational mesh for CFD simulation of velocity field and mass transport in the fully configured AERF cabin. a) (left) axial perspective view of mesh density, b) (upper right) close-up of gasper plenums, c) (lower right) seat surface mesh density.
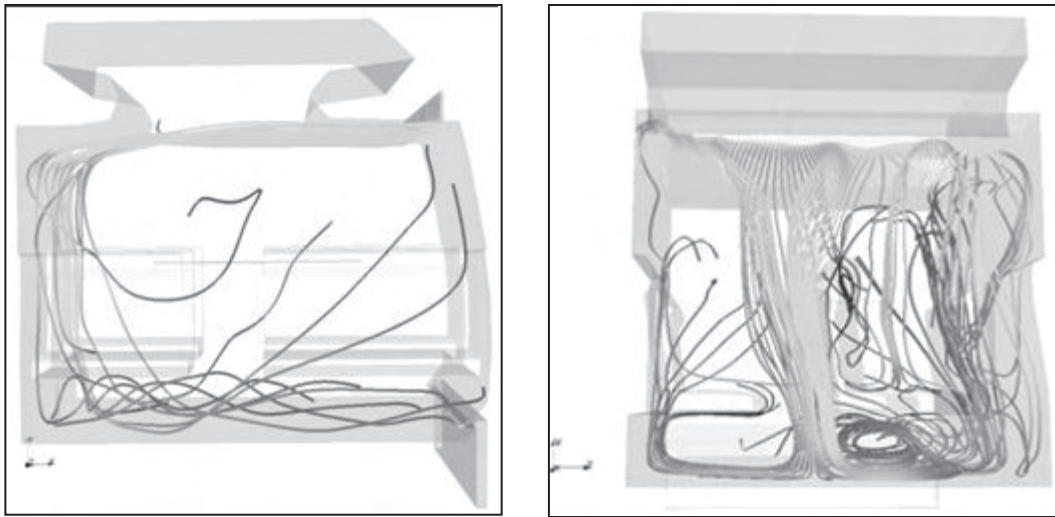
Figure 40. Fluent generated ventilation velocity vector field stream tubes, colored by speed, in fully configured AERF cabin section with both overhead luggage carriers, mesh with carrier trip strip, steady turbulent flow, TKE closure model. a) (left) axial perspective, b) transverse perspective.
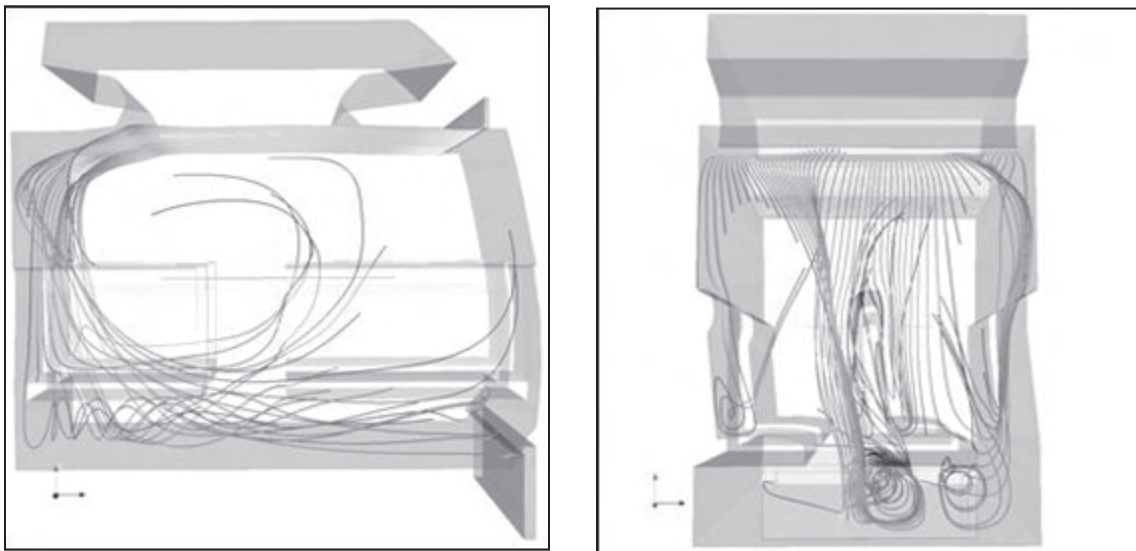
Figure 41. Star CD generated ventilation velocity vector field stream tubes, colored by speed, in fully configured AERF cabin section with both overhead luggage carriers, mesh with carrier trip strip, steady turbulent flow, TKE closure model. a) (left) axial perspective, b) transverse perspective.
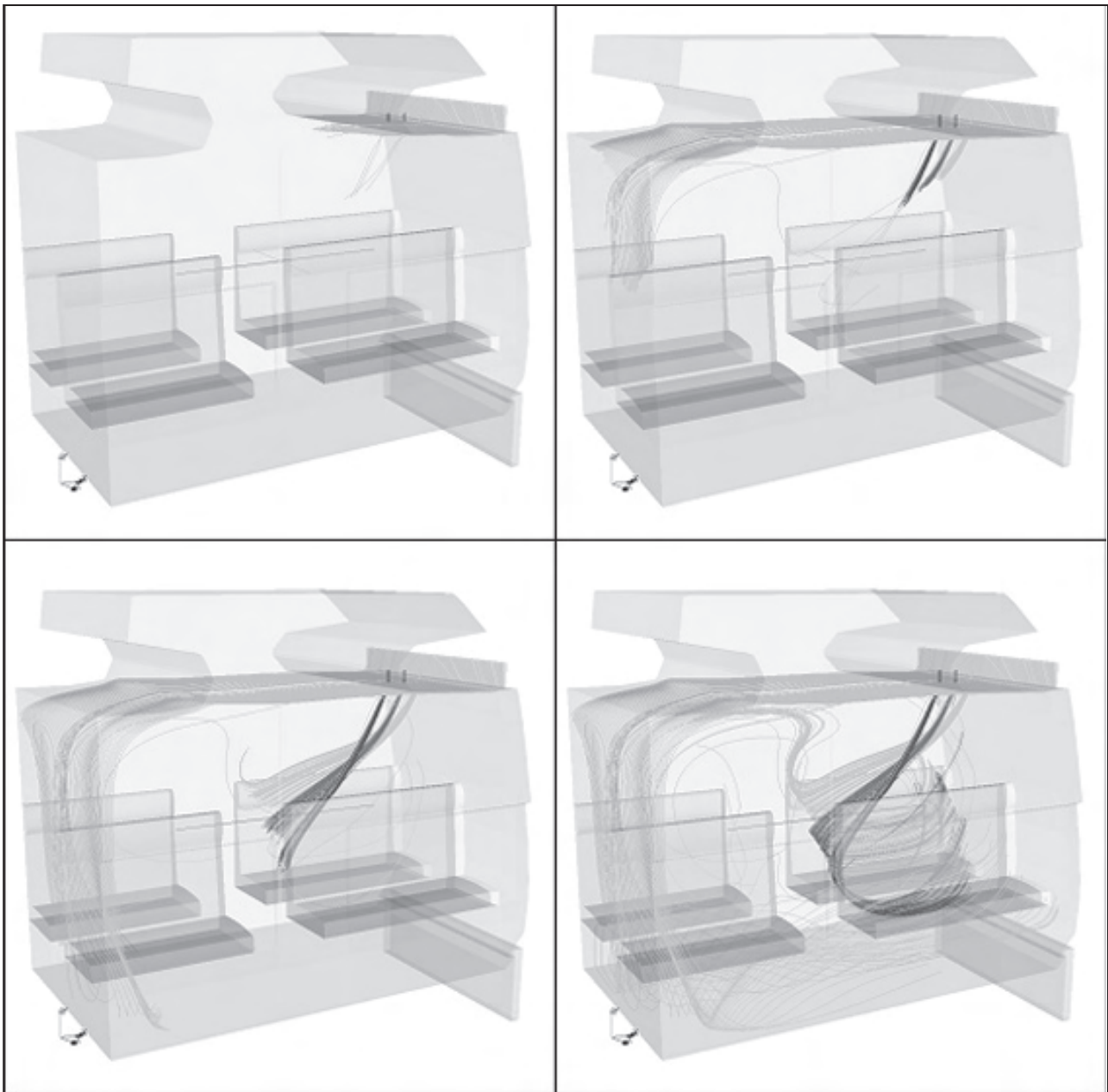
Figure 42. Star CD generated gasper vector stream tube evolution, colored by gasper, in fully configured AERF cabin section with both overhead luggage carriers, mesh with carrier trip strip, steady turbulent flow, TKE closure model.

Figure 43. Star CD generated gasper vector stream tube evolution, colored by gasper, non-vertical gasper plenum orientations, in fully configured AERF cabin section with both overhead luggage carriers, mesh with carrier trip strip, steady turbulent flow, TKE closure model.

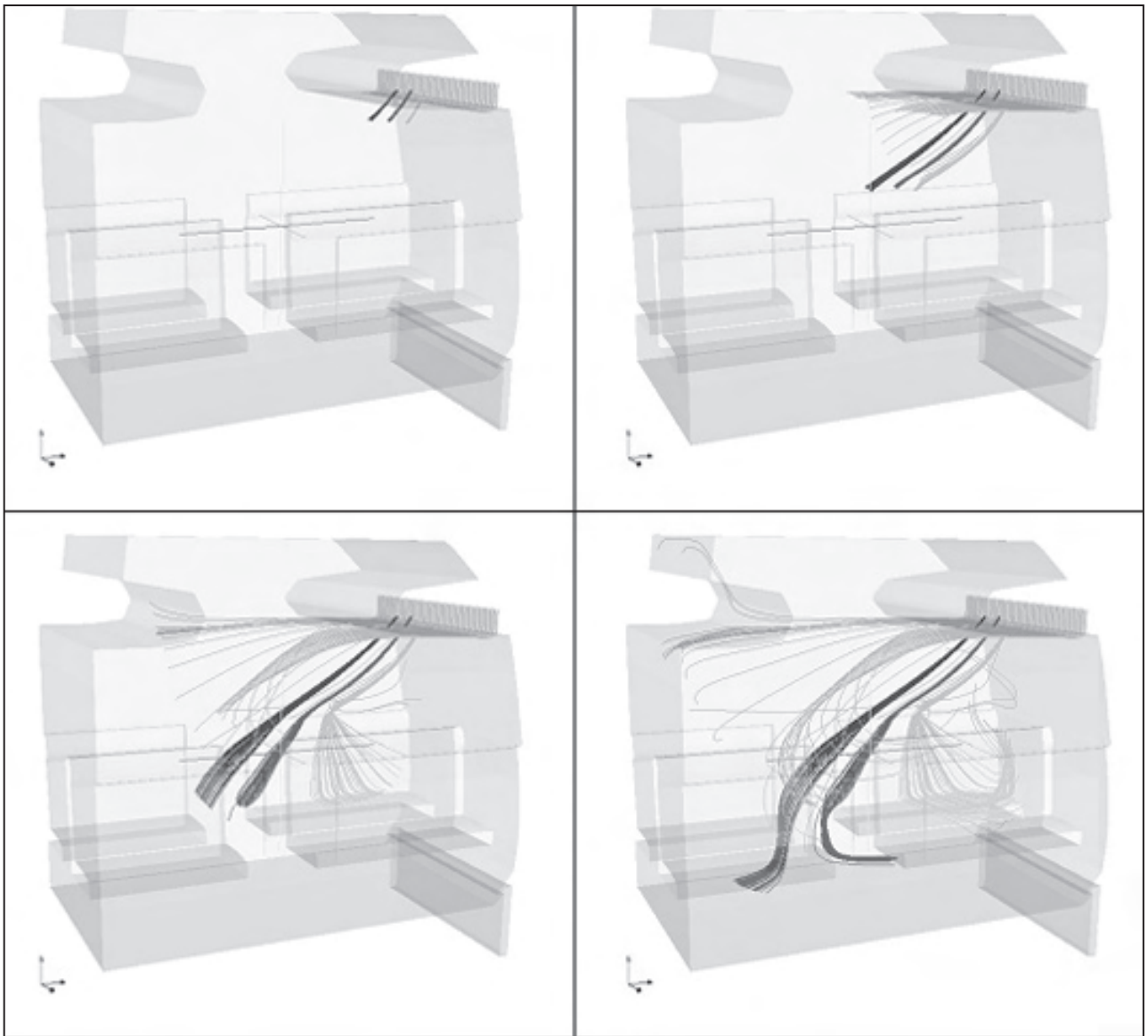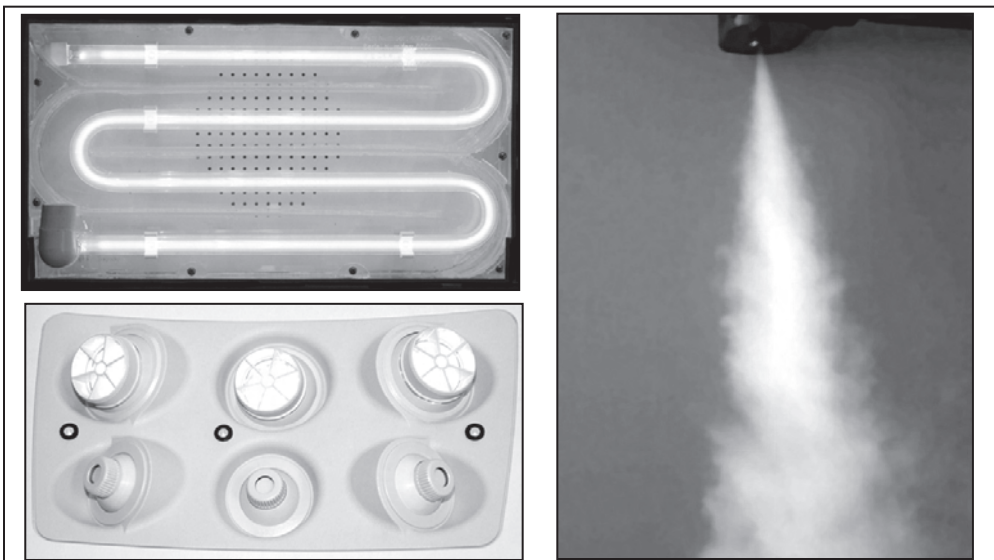**Figure 44.** BE Aerospace concept for introduction of irradiated gasper air flow. a) (top left) treatment system in passenger control unit, b) (lower left) face of passenger control unit, c) (right) gasper flow visualization experiment.

reading, preceding the first and second non-zero readings, each of which is separated by the 10-s experimental data rate. The input laminar binary diffusion coefficients d for the research code are therein denoted "DIFF," while the commercial code TKE executions are graphed for both the genuine (RND) and modified (SQR) injection geometries. Very poor correlation with the experimental data accrues to this normalization at all but the set point.

Figure 37 recreates this comparison for the CFD predictions normalized at the first non-zero experiment value at the second sample point (044,072,108). On all except the set-point graph, the smallest laminar binary diffusion coefficient solution is furthest from the data, as expected. The commercial code solutions for both genuine and modified injection geometries, and those generated by the research code for mid-range binary diffusion coefficients nominally overlay each other at the two mid-trajectory experimental locations. At the furthest downstream trajectory data station, these binary diffusion specification simulations produce solutions spanning the experimental data, while the commercial code solutions lie closest to the 10 s data point.

Fully configured cabin velocity field CFD experiments

All measurements and CFD assessments reported to this point were performed for the AERF devoid of seat rows. The original plan was to continue with experiments in the AERF fully configured with seat rows and to assess the impact of gasper operation, the design of which was to be guided by the results of CFD predictions. These precursor CFD simulations have been completed, yielding quantitative prediction of alterations to AERF ventilation flowfield distributions anticipated to be measured experimentally.

The CFD solution domain transverse span remains the half-cabin, with the longitudinal span containing the equivalent of two seat rows. Perspective views of the associated solution domain are given in Figures 38a)-b). Note that the fore- and aft-domain planes transect the seat row back, the location of which was a specifically selected application of vanishing normal derivative BCs, as appropriate for the assumption of negligible cabin axial velocity component. The cabin ventilation supply and exhaust plenums are clearly visible (Figure 38a), as are the plenums for the three gaspers, shown therein.

This CFD solution domain was discretized into a non-uniform mesh of purely hexahedral cells containing the order 2.25 million nodes, fully blocked for parallel computing. The transverse plane nodal density in the wall-free jet region, Figure 39a), emulates that of the mesh refinement study. Since gasper operation corresponds to the classic jet in crossflow, further nodal densification was added in regions where gasper flows interact with the wall jet. Figure 39b) presents a magnified view of the internal geometry and meshing in the gasper plenum terminus – wall jet region. Finally (Figure 39c) illustrates mesh density on the surface of the seat rows.

Two variations of this mesh were generated, one with luggage carrier sharp terminus and the second with the tangent approximation to its genuine curvature, recall Figure 16. As expected, the steady TKE model CFD solutions generated by both commercial codes suffered the error detected for the empty cabin simulation, i.e., generation of a single circulation region due to failure of the wall jet to separate at the luggage carrier terminus.

For the sharp carrier terminus, both commercial code TKE solutions predict wall jet separation in agreement with the totally time-averaged experimental data, hence produce cabin dual circulation patterns. For two perspective orientations, Figures 40a)-b) and 41a)-b) summarize these steady velocity field solutions in terms of flow stream tubes colored by speed. There exist no surprises in these solutions, each of which predicts anticipated flow deflection by the seat backs and generation of additional tubular circulation regions between the seat undersides and the cabin floor.

CFD simulation of the operation of the gaspers with the ventilation supply flow concludes this project component. The nominal exit velocity for a full-open gasper is order 15 m/s, nominally an order of magnitude larger than that of the local wall jet, through which each must penetrate. Nevertheless, the CFD simulation results confirm that significant deflection of the gasper flows occurs in penetrating the wall jet. Figures 42a)-d) presents time evolution of the stream tube trajectory of the three gasper jets, color-coded for origin, for the direction of injection vertical. It is clear that the first jet suffers the greatest deflection from vertical, and that each successive gasper jet is accordingly shielded by its predecessor.

Of course, gasper flow direction is individually adjustable by each seated occupant, so is readily redirected to the correct seat location. Figures 43a) – d) illustrate the results of successively adjusting each gasper plenum chamber axis from the vertical, such that the gasper flow trajectories are now nominally parallel.

Fully configured cabin mass transport CFD experiment

A Cooperative Research and Development Agreement was established between the FAA CAMI and BE Aerospace to evaluate their concept of a rapid air exchange response system, should a toxic substance released into an aircraft cabin be detected. The BEA innovation involved a modification to the cabin gasper plenum system in each overhead passenger control unit. The concept

was to rapidly generate a "good air envelope" over each seated passenger via subjecting the gasper airflow to strong ultra-violet radiation prior to issuing it from the control unit. Figure 44a)-c) illustrates the design essence of this system.

The key characterization sought was estimation of the time evolution of the gasper flow envelope as directed towards a seated occupant. The associated AERF experiment was designed and some initial data recorded, but the experimental study was not completed. For the cabin ventilation flow at the steady TKE solution, shown in Figure 41, the results of a cursory CFD experiment are summarized in Figure 45 as time evolution of the envelope of mass emanating from the center gasper in the AERF passenger control unit. In the absence of a seated mannequin to deflect the flow, the gasper is directed to the seat back. Within 1 sec, the contour of 5% treated air touches the seat back and thereafter does not penetrate significantly further. The contour of 1.5% treated air envelopes the seat front and back by 2 s; thereafter, these solution profiles remain essentially unchanged through 7 s of simulation time. No further CFD experiments were conducted, as project funding drew to a close.

SUMMARY, CONCLUSIONS, AND RECOMMENDATIONS

Summary

The aircraft ECS-generated cabin ventilation velocity vector field CFD validation exercise was enabled by acquisition of high-quality, time-accurate 3-dimensional experimental data for the cabin velocity vector distribution in the Boeing 747-100 AERF and a Boeing 747-400 in flight. These data clearly confirm and quantify the existence of a time-dependent, turbulent velocity vector field, constituted of a large-cabin proper circulation pattern and a second smaller circulation region bounded by the luggage carriers. This flowfield is energized by unsteady Coanda-effect wall jet separation from the underside of the cabin sidewall luggage carrier curved terminus.

For two commercial codes, the TKE closure model steady solution process is exceptionally efficient in generating a time-independent, velocity-vector field. Conversely, a time-accurate, CFD simulation solution process appears required, which is much more demanding on computer resources. The combined use of commercial and proprietary CFD codes did yield qualitative and quantitative assessments of factors influencing CFD simulation velocity vector field fidelity.

The disturbing factor with the commercial code TKE steady solutions is that qualitative agreement with the completely time-averaged experimental data occurred only for the insertion of a tangent discontinuity at the luggage carrier terminus. The mesh refinement study confirmed that, with sufficient mesh resolution to accurately define the correct carrier terminus, the wall jet did not separate but, instead, remained attached, yielding a single cabin circulation pattern at odds with the data. The requirement for use of a mesh "trip strip" appears dominated by the steady flow iteration strategy employed by these codes. The true value of such a rapidly generated TKE solution appears as an initial condition for a following time-accurate, unsteady CFD simulation. Specifically, the time-accurate research code CFD simulation generated a time-dependent solution in good qualitative and promising quantitative agreement with the experimental data, including a frequency analysis.

The validation exercise for mass transport aircraft generated results that were challenging to interpret but were, nevertheless, very informative. The dominant contributing factor was experimental data unreliability, the result of the sampling rate being too slow in comparison with the circulation time within the cabin. This issue was further complicated by the overall ventilation flowfield unsteadiness, which resulted in experimental data fluctuation spread on the order of the mean, therefore the mean is a non-representative data summary. The inability to firmly quantify VHP mass fraction in the injection stream entering the cabin was an additional challenging factor. Nevertheless, the combination of commercial and research code CFD experiments did generate clear assessments of the balance between flow convective-diffusive and CFD algorithm/code dissipative mechanisms, both physical and numerical, in predicting of the time evolution of mass fraction distributions in the AERF.

Conclusions

The ECS-generated aircraft cabin ventilation velocity vector field CFD validation exercise is deemed very successful. A firm knowledge base now exists for characterizing factors affecting the fidelity of time-accurate, 3-dimensional CFD predictions of ventilation velocity vector flowfields in the AERF. The established sonic anemometer experimental data protocol is confirmed to be highly appropriate in supporting the validation requirement.

The validation exercise for CFD prediction of mass transport was less conclusive, due principally to limitations inherent in the experimental measurement protocol. Notwithstanding, specifically designed and executed computational experiments did provide clear insight into mechanisms dominating CFD time-dependent, mass transport simulation fidelity, hence design of an improved experimental protocol.
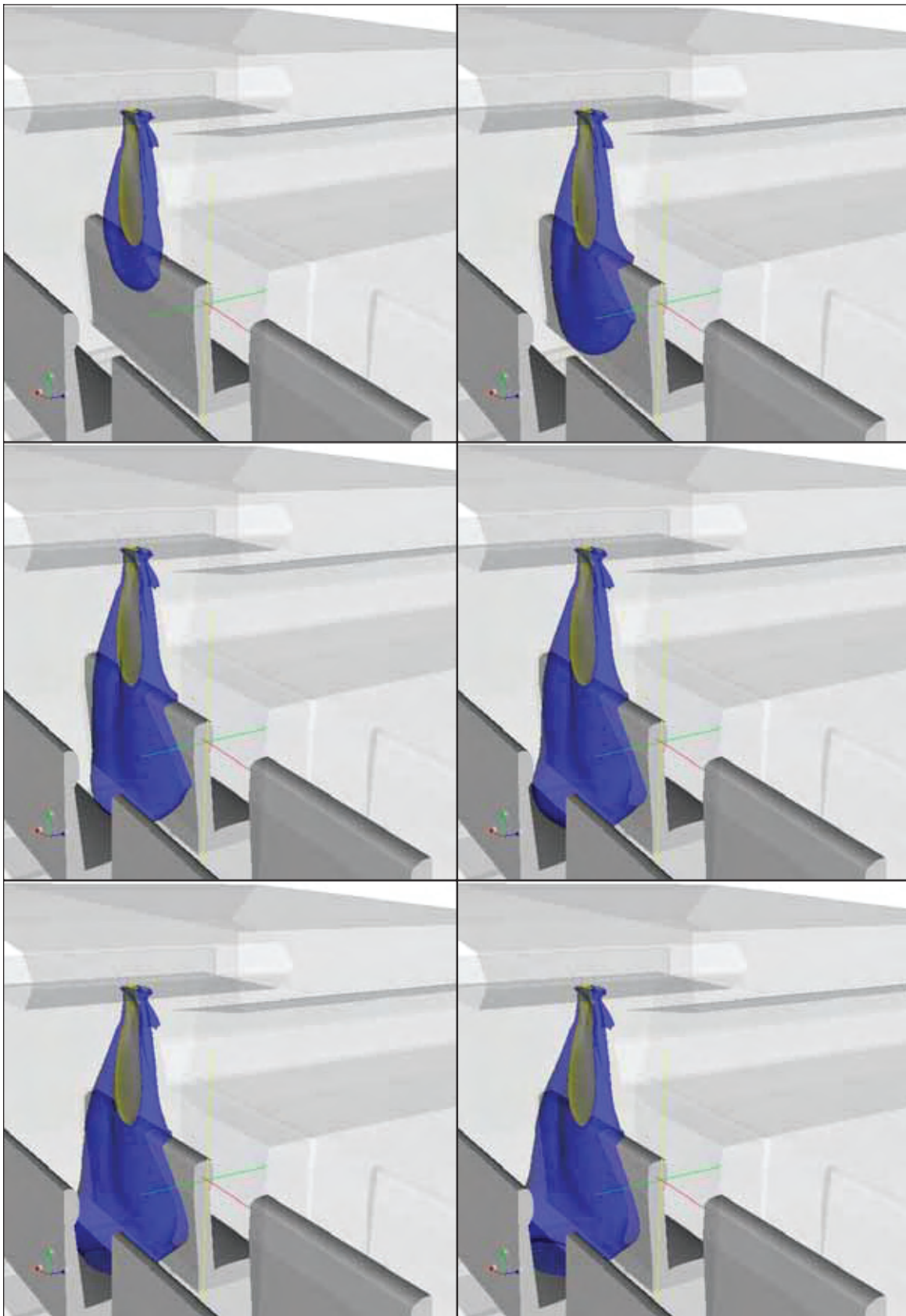
Figure 45. Star CD generated gasper flow envelope evolution, central gasper only operating in fully configured AERF cabin section with both overhead luggage carriers, mesh with carrier trip strip, steady turbulent flow, TKE closure model, yellow contour at 5%, blue contour at 1.5 %, time interval 1 < *t* < 7 s.

The CFD computer demand distinction between the commercial steady RaNS codes and select time-accurate algorithms/codes is clearly a dominating factor in mass transport simulation in aircraft ventilation flowfields. Combining these capabilities appears to be the required approach, with steady code results, properly interpreted and generated, producing initial conditions for the ensuing time-accurate mass transport CFD simulation.

Recommendations

The CAMI AERF is an exceptionally valuable research facility to support research on the fate of pathogens introduced into aircraft cabin ventilation flowfields. The requirements are clearly delineated for the acquisition of quality velocity and mass transport experimental data to support CFD validation requirements. The astute use of CFD methodology can certainly generate precise design guidance for such experiments, effectively and efficiently reducing the size of the data matrix required to serve the validation requirement. The results of this steadily growing knowledge base will predict estimation of optimal opportunities for onboard sensor locations, hence will support associated hypotheses for examining potential damage mitigation strategies, should a cabin release event be detected.

REFERENCES

1. Kelso, R. M., Roy, S. & Baker, A. J., "CFD Prediction of Thermal Comfort Distributions in a 3-D Space With High Ventilation Rates," in Seppanen, O. et al. (eds), *Indoor Air* '93: 6th Int. Conf. on Indoor Air Quality and Climate, V. 5, Helsinki Tech. Univ. Press, Finland, p. 313-8, 1993.

2. Nielsen, P.V., "Prediction of Air Flow and Comfort in Air Conditioned Spaces**,**" *ASHRAE Transactions*, V. 81, Part 2, 1974.

3. Lemairc, A. D., Ed**,** *Room Air and Contaminant Flow Evaluation of Computational Methods, Summary*, International Energy Agency, Annex 20, 1992.

4. Moser, A, Director, *International Energy Agency Annex 26: Energy Efficient Ventilation of Large Enclosures*, ETH Zurich, 1992.

5. Baker, A. J., Williams, P.T., & Kelso, R. M. , "Numerical Calculation of Room Air Motion, I. Math, Physics and CFD Modeling," *ASHRAE Transactions*, V.100, Pt. 1, p.514-30, 1994.

6. Williams, P.T., Baker, A. J., & Kelso, R. M. , "Numerical Calculation of Room Air Motion, II. the Continuity Constraint FE Method for 3-D Incompressible Thermal Flows," *ASHRAE Transactions*, V.100, Pt. 1, p.531-48, 1994.

7. Williams, P.T., Baker, A. J., & Kelso, R. M. , "Numerical Calculation of Room Air Motion, III. 3-D CFD Simulation of a Full Scale Room Air Experiment," *ASHRAE Transactions*, V.100, Pt. 1, p.549-64, 1994.

8. Williams, P. T. & Baker, A. J., "CFD Characterization of 3-D Natural Convection in a Two-Cell Enclosure with a Door," *ASHRAE Transactions*, V. 100, Pt. 2, p.685-96, 1994.

9. Murakami, S. Kato, S, & Kondo, Y., "Numerical Prediction of Horizontal Non-Isothermal 3-D Jet in Room Based on Algebraic 2nd Moment closure Model," ASHRAE Tech Paper, AN-92-9-3, 1992.

10. Baker, A. J., Winowich, N.S., Taylor, M.B. & Heller, M. R., "Prediction of the Distribution of Indoor Air Quality and Comfort in Aircraft Cabins Using Computational Fluid Dynamics (CFD**)**," in N.L. Nagda, ed. *Air Quality and Comfort in Airliner Cabins*, ASTM SP 1393, p. 117-34, 2000.

11. Jones B.W., Hosni, M..H., & Meng, H., "The Interaction of Air Motion and the Human Body in Confined Spaces," ASHRAE Research Project 978 Final Report, 2001.

12. Ericson, S. C., Wong, K.L. , Orzechowski, J. A., Baker, A. J., Garner, R. P. & McCloskey, T. S., "CFD Validation for Contaminant Transport in Aircraft Cabin Ventilation Flowfields," Proceedings, 7th *Intl. Sym. on Ventilation for Contaminant Control*, Sapporo, Japan, 2003.

13. Baker, A. J., Roy, S. & Kelso, R. M., "CFD Experiment Characterization of Airborne Contaminant Transport for Two Practical 3-D Room Air Flowfields," *Building. & Environment*, V. 29, p. 253-59, 1994.

14. Memarzadeh, F., *Assessing the Efficacy of Ultraviolet Germicidal Irradiation and Ventilation in Removing Mycobacterium Tuberculosis*, National Institutes of Health (NIH) Handbook, 2000.

15. Baker, A. J., Kelso, R. M., Gordon, E. B., Roy, S., & Schaub, E.G., "Computational Fluid Dynamics: A Two-Edged Sword," *ASHRAE Journal*, V. 39, No. 8 , p. 51-8, 1997.

16. Williams, P. T. & Baker, A. J., "Incompressible Computational Fluid Dynamics and the Continuity Constraint Method for the 3-D Navier-Stokes Equations," *Journal of Numerical Heat Transfer*, Part B*, V29, p.137-273, 1996.

17. Chaffin, D. J. & Baker, A. J., "On Taylor Weak Statement Finite Element Methods for Computational Fluid Dynamics," *International Journal of Numerical Methods in Fluids,* V. 21, p.273-94, 1995

18. Kolesnikov, A. & Baker, A. J., "An Efficient High Order Taylor Weak Statement Formulation for the Navier-Stokes Equations," *Journal of Computational Physics*, V. 173, p. 549-74, 2001.

19. Wilcox, D. C., *Turbulence Modeling for CFD*, 2nd Ed, DCW Industries, 2000.

20. Pope, S. B., *Turbulent Flows*, Cambridge University Press, 2000.

21. Spalart, P.R. and Allmaras, S.R., "A One-Equation Turbulence Model for Aerodynamic Flows," AIAA Technical Paper 92-0439, 1992.

22. Moin, P. & Mahesh, K., "Direct Numerical Simulation: A Tool for Turbulence Research," *Annual Review of Fluid Mechanics*. V30, p.539-78.

23. Fluent, Inc. CFD Flow Modeling Software and Services. [www.fluent.com]. 12/8/2004.

24. CD-adapco, Inc. Star-CD Flow Modeling Software and Services. [http://us.adapco.com]. 12/8/2004.

25. Wong, K.L. A Parallel Interoperable Computational Mechanics System Simulator (PICMSS). [www.picmss.org]. 12/8/2004.

26. PSE CFD Lab Academic Research CFD Code. [http://cfdlab.utk.edu/Internet courses/ES552w/PSEs]. 12/8/2004.

27. Campbell Scientific, Inc. Wind Speed and Wind Direction Sensors. 2/17/2004. [www.campbellsci.com/wind.html#csat].12/20/2004.

28. Thomas, Jim, "FAA/CAMI On-Site Testing in a 747 Fuselage Section, Project 81051." Strategic Technology Enterprises Technical Report, April 2004.

29. Guided Wave Incorporated. H2O2 Monitor. [www.guided-wave.com/h2o2_monitor.htm]. 12/20/2004.

30. National Instruments Corporation. LabVIEW – The Software That Powers Virtual Instrumentation – Products and Services. 2004. [www.ni.com/labview]. 12/8/2004.